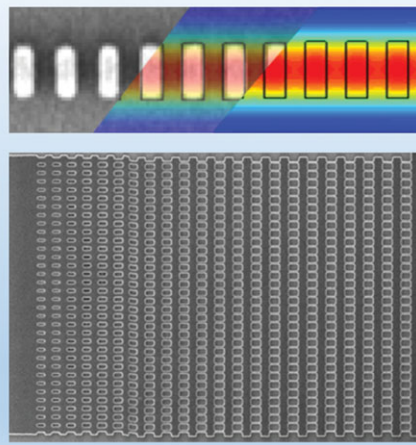


INTERNATIONAL
YEAR OF LIGHT
2015REVIEW
ARTICLE

Abstract Periodic structures with a sub-wavelength pitch have been known since Hertz conducted his first experiments on the polarization of electromagnetic waves. While the use of these structures in waveguide optics was proposed in the 1990s, it has been with the more recent developments of silicon photonics and high-precision lithography techniques that sub-wavelength structures have found widespread application in the field of photonics. This review first provides an introduction to the physics of sub-wavelength structures. An overview of the applications of sub-wavelength structures is then given including: anti-reflective coatings, polarization rotators, high-efficiency fiber-chip couplers, spectrometers, high-reflectivity mirrors, athermal waveguides, multimode interference couplers, and dispersion engineered, ultra-broadband waveguide couplers among others. Particular attention is paid to providing insight into the design strategies for these devices. The concluding remarks provide an outlook on the future development of sub-wavelength structures and their impact in photonics.



Waveguide sub-wavelength structures: a review of principles and applications

Robert Halir^{1,2,*}, Przemek J. Bock³, Pavel Cheben⁴, Alejandro Ortega-Moñux^{1,2},

Carlos Alonso-Ramos¹, Jens H. Schmid⁴, Jean Lapointe⁴, Dan-Xia Xu⁴,

J. Gonzalo Wangüemert-Pérez¹, Íñigo Molina-Fernández^{1,2}, and Siegfried Janz⁴

1. Introduction

Sub-wavelength periodic structures are arrangements of different materials with a pitch small enough to suppress the diffraction effects arising from their periodicity. They have been known in electromagnetism since Hertz carried out his pioneering experiments on radio waves in the late 19th century [1]. He used a spark transmitter and detector embedded in cylindrical metal mirrors to boost the signal (see Fig. 1). To study the polarization of the waves he employed a grid of wires with a pitch much smaller than the wavelength. Such a device blocks transmission when oriented parallel to the polarization direction of the wave, but has virtually no effect when it is positioned perpendicular to the polarization direction. As will be discussed later, this presently well-known effect arises directly from the sub-wavelength nature of the device. Lord Rayleigh theoretically studied periodically structured media [2], and was the first to predict the birefringence effect now known as “form birefringence” in an array of parallel dielectric

cylinders. However, it was not until the 1940s that electromagnetic wave propagation in a medium structured at the sub-wavelength scale was studied for alternating layers of a dielectric and a metal [3]. In the 1950s a comprehensive theoretical study of sub-wavelength structures was developed by Rytov [4], who showed that these structures can behave as homogeneous media with an equivalent refractive index that depends on their geometry and the polarization state of the incident wave. Optical sub-wavelength structures were discovered in the 1960s by Bernhard and Miller in the cornea of night-flying moth eyes [5]. This structure reduces reflections from the eyes as a camouflage mechanism protecting the species from nocturnal predators. Inspired by this “moth-eye” structure, Clapham and Hutley fabricated optical sub-wavelength structures with anti-reflective properties in the early 1970s [6]. The sub-wavelength phenomenon has been extensively exploited in free-space optics [7], including birefringence optics and polarizers [8,9] and anti-reflection surfaces [10–12]. Birefringent sub-wavelength structures were proposed for nonlinear

¹ Universidad de Málaga, Dept. de Ingeniería de Comunicaciones, ETSI Telecomunicación, Campus de Teatinos s/n, 29071 Málaga, España

² Bionano Center for Nanomedicine and Biotechnology, Parque Tecnológico de Andalucía, 29590 Málaga, España

³ CMC Microsystems, Kingston, Ontario, K7L 3N6, Canada

⁴ National Research Council of Canada, Ottawa, Ontario, K1A 0R6, Canada

*Corresponding author: e-mail: robert.halir@ic.uma.es

This is an open access article under the terms of the Creative Commons Attribution-NonCommercial-NoDerivs License, which permits use and distribution in any medium, provided the original work is properly cited, the use is non-commercial and no modifications or adaptations are made.

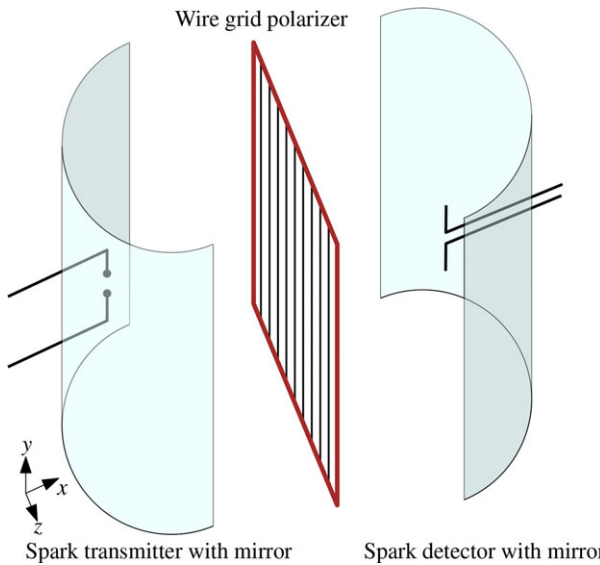


Figure 1 Schematic of Hertz's experiments on the polarization of radio waves using a sub-wavelength wire grid polarizer. If the grid orientation is perpendicular to the polarization axis of the wave, transmission is unaffected; if it is parallel, transmission is blocked.

frequency conversion by Van der Ziel [13] and experimentally demonstrated in GaAs waveguides [14].

However, it has been with more recent development of photonic technologies and high-resolution lithography that sub-wavelength structures have seen widespread application in integrated optics. Currently these structures are employed to synthesize a wide range of refractive indexes simply by lithographic patterning [15], to optimize fiber-chip grating couplers [16], vertical-cavity surface-emitting lasers (VCSELs) [17], and wavelength multiplexers [15], and to design low-loss waveguide crossings [18], high Q -factor resonators [19], and ultra-broadband multimode interference (MMI) couplers [20], among other applications.

This review aims to provide the reader with a solid understanding of the physics of sub-wavelength structures and provide an extensive overview of their applications. Given this focus on sub-wavelength structures, there is a series of topics related to the fundamentals of resonant structures that will not be covered here, but for which extensive review papers or books are available. Some of the topics that are not discussed are: diffraction gratings [21–23], resonant waveguide gratings [24], Fano resonances [25], and Bragg gratings [26]. However, the *application* of sub-wavelength structures to the design of some diffractive elements is described, including fiber-to-chip grating couplers and wavelength multiplexers.

The paper is organized as follows. Section 2 describes the sub-wavelength behavior of periodic structures. For the sake of clarity this discussion is divided into structures arrayed crosswise and lengthwise to the direction of propagation. The same classification is maintained when presenting the applications of sub-wavelength structures in Sections 3 and 4. Throughout the text the term sub-wavelength grating is often used to refer to sub-wavelength structures.

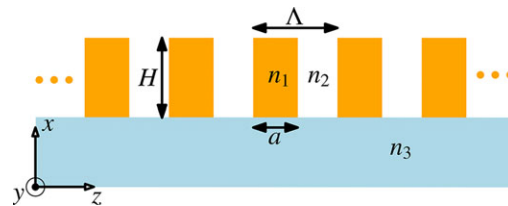


Figure 2 Schematic of a z -periodic dielectric waveguide, with n_1 , n_2 , and n_3 being the refractive indexes of the core, cladding, and substrate materials (typically $n_1 > n_2, n_3$). For the purpose of this review two types of structures are considered: crosswise structures where light travels along the x or y direction, and lengthwise structures where light travels along the z direction.

2. The sub-wavelength regime

Consider the periodic waveguide structure shown in Fig. 2 which consists of rectangles of refractive index n_1 spaced at a pitch Λ at the boundary of two media with refractive indexes n_2 (superstrate, or upper cladding) and n_3 (substrate, or lower cladding). The duty cycle of the structure is a/Λ and the thickness of the core layer is H . Many applications of sub-wavelength structures use the silicon-on-insulator waveguide platform, where the waveguide core material is silicon, $n_1 \sim 3.5$, the bottom cladding is silicon oxide, $n_3 \sim 1.45$, and the upper cladding is silicon oxide, a polymer, or air, so that $n_2 \sim 1\text{--}1.6$. This results in sub-wavelength pitches of the order of $\Lambda \sim 300$ nm for a free-space wavelength $\lambda \sim 1.55$ μm .

The electromagnetic properties of the periodic structures considered here are fully described by the theory developed for photonic crystals [27]. However, for the purpose of this review, a much simpler theory that provides intuitive guidelines for the design process will be used. The periodic structure shown in Fig. 2 can generally operate in the following regimes, depending on the ratio between the structure's pitch (Λ) and the free-space wavelength (λ): (i) diffraction, where the incoming beam is scattered in different orders; (ii) reflection, where the incoming beam is reflected backwards; and (iii) sub-wavelength, where diffraction effects due to the periodicity of the structure are suppressed.

In the following the conditions for sub-wavelength operation will be examined, and the behavior of the structure will be described in more detail. For the purpose of this paper, this discussion is divided in two cases: (i) light propagating crosswise through the grating (propagation along the x or y axis in Fig. 2) and (ii) light propagating lengthwise through the grating (propagation along the z axis in Fig. 2).

2.1. Crosswise periodic structures

Consider that light is incident on the structure shown in Fig. 2 in the x direction. From the scalar grating equation, the angle of the diffraction orders (θ_k) is given by $n_d \sin \theta_k = k\lambda/\Lambda$, with $n_d = \{n_2, n_3\}$ for diffraction into the cladding and the substrate, respectively [28]. Diffraction effects will

thus be suppressed for all orders $|k| \geq 1$ when $|\sin \theta_{\pm 1}| > 1$, that is when

$$\lambda/\Lambda > n_d = \max\{n_2, n_3\}. \quad (1)$$

Throughout this paper a periodic structure where all diffraction orders $|k| \geq 1$ are suppressed is referred to as a sub-wavelength grating (SWG). This structure can be approximated as an equivalent homogeneous medium if the following additional conditions are fulfilled:

- At the operation wavelength and for the considered polarization, the grating should support only a single waveguide array mode propagating along the x direction in Fig. 2. A detailed discussion of this condition, which may lead to a more restrictive condition for the ratio λ/Λ compared to Eq. (1), can be found in [29].
- The grating should be thick enough so that the evanescent modes that are created at the top and bottom grating interfaces do not tunnel through the grating region.

If all the above conditions are simultaneously satisfied, the SWG can be modeled as an equivalent homogeneous material. If the grating extends indefinitely in the x and y directions and $\lambda \gg \Lambda$ (deep-sub-wavelength regime), the refractive index of the equivalent homogeneous medium is given by Rytov's formulas [4]:

$$n_{\parallel}^2 = \frac{a}{\Lambda} n_1^2 + \left(1 - \frac{a}{\Lambda}\right) n_2^2 \quad (2)$$

$$\frac{1}{n_{\perp}^2} = \frac{a}{\Lambda} \frac{1}{n_1^2} + \left(1 - \frac{a}{\Lambda}\right) \frac{1}{n_2^2} \quad (3)$$

for polarization parallel (along the y direction) and perpendicular (along the z direction) to the interfaces between the alternating layers. Note that for a given duty cycle $n_{\parallel} > n_{\perp}$, so that SWGs are intrinsically birefringent. Rytov's formulas are derived using a zero-order approximation, i.e. assuming that the ratio $\lambda/\Lambda \rightarrow \infty$. Higher order approximations that improve the accuracy of Rytov expressions for smaller values of λ/Λ can be found in [30, 31].

Rytov's formulas provide a valuable start point for many designs, even when the conditions outlined above are not rigorously fulfilled. For a precise design, the SWG cannot generally be treated as a simple homogeneous medium and numerical analysis is required. In particular, when the structure is finite in the z and y directions waveguiding effects need to be taken into account, and the model of the SWG will depend on the properties of the waveguide mode propagating through the structure. Note that for the crosswise geometry considered in this section the waveguide modes can be obtained with a conventional mode solver.

Finally consider the special case where the $k = \pm 1$ diffraction orders are diffracted at grazing incidence, i.e. in the $\pm z$ direction. Equation (1) then reads $n_d = \lambda/\Lambda$, i.e. the grating operates with a “near-wavelength” pitch. In this case n_d actually corresponds to the effective index of the guided waveguide (Bloch) mode traveling in the $\pm z$ direction (a detailed discussion on Bloch modes can be found

in Section 2.2). The (leaky) waveguide mode in turn couples light back to a radiated mode producing potentially strong back-reflections from the grating surface [32]. This phenomenon, which is also referred to as guided mode resonance, was initially investigated because it is responsible for Wood anomalies in diffraction gratings [33]. Golubenko et al. showed that when this type of grating is formed in a dielectric waveguide it can exhibit a resonant response in its reflectivity as a function of wavelength and angle of incidence [34]. Baets and co-workers demonstrated high reflectivity and polarization selectivity at normal incidence for surface relief gratings in a semiconductor-air interface [35, 36]. These devices, which were named as “giant reflectivity to order zero” (GIRO) gratings, were proposed to act as reflective mirrors in VCSELs. Further development of this concept resulted in high-refractive-index rods surrounded by a single low-index material (i.e. $n_2 = n_3 \ll n_1$ in Fig. 2) yielding reflectivities approaching 100% for a broad spectral bandwidth [37, 38]. In this case the structure is often referred to as a high-contrast grating (HCG).

2.2. Lengthwise periodic structures

When light travels through the structure shown in Fig. 2 in the z direction, it is index-guided laterally (x direction). Such a structure behaves as a periodic segmented waveguide, so a convenient description of its behavior can be obtained using the Bloch–Floquet formalism described in [26]. Since this structure is periodic only in the longitudinal z direction, but not in the transversal x and y directions, supercell methods are not appropriate for the numerical analysis, and optimized numerical tools should be utilized [39–47]. Light propagating in a segmented waveguide adapts to the periodicity as Bloch–Floquet modes of the periodic structure, with a mechanism that is formally similar to electron propagation in periodic crystals. Propagation of a Bloch mode through a z -periodic waveguide can be expressed as $E(x, z + \Lambda) = E_B(x, z) \exp(-\gamma_B \Lambda)$, where $E_B(x, z)$ is the Bloch mode field distribution within a single period and γ_B is its complex propagation constant. In general, $\gamma_B = \alpha_B + j k_B = \alpha_B + j(2\pi/\lambda)n_B$, where α_B and k_B are the attenuation and propagation constants and n_B is the effective index of the Bloch mode.

For a given pitch, Λ , the behavior of a periodic waveguide is highly dependent on operating frequency, ω , or equivalently the free-space wavelength, λ . Figure 3a shows a schematic k – ω diagram of a periodic waveguide [48]. For low frequencies ($\omega < \omega_1$), the propagation constant (k_B) grows monotonically, indicating that the periodic waveguide behaves as a conventional waveguide. Propagation through a periodic waveguide in this sub-wavelength regime is illustrated in Fig. 4a. In the frequency range corresponding to the photonic bandgap ($\omega_1 < \omega < \omega_2$), light cannot propagate through the structure and Bragg reflection occurs (Fig. 4b). In this regime k_B is constant, $k_B^{\text{Bragg}} = \pi/\Lambda$. Above the first bandgap, the Bloch–Floquet mode becomes leaky and light is partially radiated out of the waveguide, as shown in Fig. 4c.

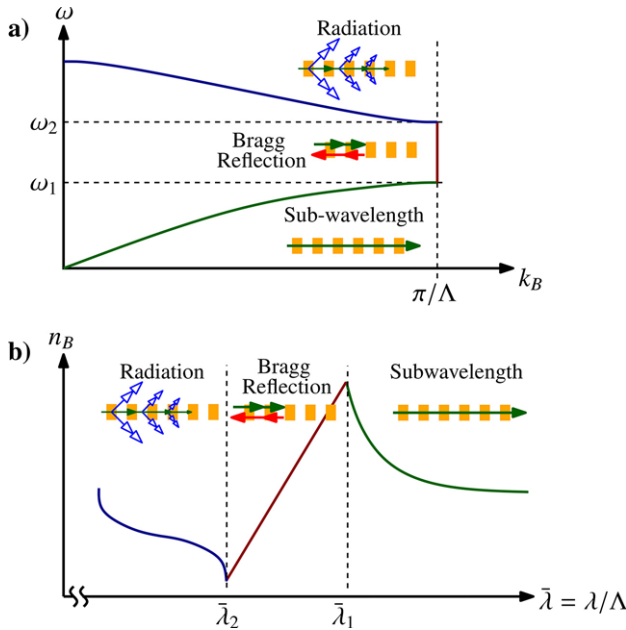


Figure 3 (a) Schematic dispersion diagram in the first Brillouin zone of a periodic waveguide with lengthwise propagation (along the z axis). (b) An equivalent representation of the Bloch mode effective index (n_B) of the periodic waveguide as a function of the wavelength-to-pitch ratio $\bar{\lambda} = \lambda/\Lambda$. Higher order diffraction and reflection bands are not shown.

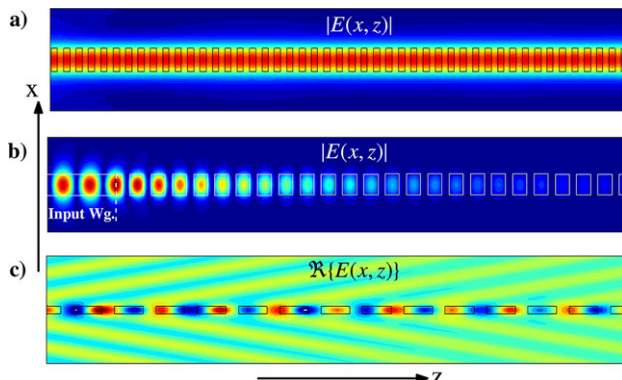


Figure 4 Propagation of light through a periodic waveguide with symmetric vertical structure, i.e. $n_2 = n_3$ (see Fig. 2). (a) In the sub-wavelength regime ($\lambda \gg \Lambda$) the structure behaves as a conventional dielectric waveguide. (b) In the bandgap light is reflected back into the uniform (non-segmented) input waveguide forming a standing wave pattern, whereas it is gradually attenuated in the periodic waveguide. (c) For wavelengths comparable to the pitch of the structure, light is radiated out of the waveguide. Only the $k = -1$ diffraction order is propagating in this figure.

For some of the applications discussed here, it is useful to re-plot the k - ω diagram of Fig. 3a as the effective index of the Bloch–Floquet mode, n_B , versus the wavelength-to-pitch ratio, $\bar{\lambda} = \lambda/\Lambda$. This results in the graph shown in Fig. 3b. In the deep sub-wavelength regime, when $\lambda \gg \Lambda$, n_B is virtually flat. As the bandgap is approached,

n_B increases, and then closely follows the linear relation $n_B^{\text{Bragg}} \sim (1/2)(\lambda/\Lambda)$ within the bandgap ($\bar{\lambda}_2 < \bar{\lambda} < \bar{\lambda}_1$). Although this linear behavior has been rigorously proven only for a two-layer periodic stratified structure [49], most periodic waveguides of practical interest exhibit this approximately linear response within the bandgap. For lower values of λ/Λ light is diffracted out of the waveguide. Although not shown here for simplicity, it should be noticed that higher order reflection and diffraction bands appear alternately for decreasing values of λ/Λ .

Before focusing on the sub-wavelength operation, some integrated optics applications of the other operating regimes will be mentioned. The bandgap is exploited, among other devices, in distributed Bragg reflectors (DBRs), which are key elements of DBR lasers [50] and VCSELs [51]. In the diffraction regime, periodic waveguides can act as fiber–chip surface grating couplers [23,52]. By judiciously designing the grating geometry, the coupling efficiency from the planar waveguide to the optical fiber situated above the chip can be maximized. The use of SWG structures to optimize grating couplers is discussed in Section 3.5.

The sub-wavelength regime is reached when the ratio of wavelength and pitch is high enough for the effective index of the Bloch–Floquet mode to drop below the Bragg threshold:

$$n_B < \frac{1}{2} \frac{\lambda}{\Lambda}. \quad (4)$$

Reflection and diffraction effects are then suppressed and the structure operates in the sub-wavelength regime. Light propagates through the SWG without losses in spite of the multiple discontinuities along the propagation direction, as shown in Fig. 4a. If the grating extends indefinitely in the x and y directions and $\lambda \gg \Lambda$ (deep-sub-wavelength regime), it can be modeled as an equivalent homogeneous medium with a refractive index given approximately by Rytov's formula (Eq. (2)) for light polarized parallel to the interfaces between the media (along the x or y axis). Higher order approximations can be found in [30,31]. This approach provides a qualitative description of the behavior of SWG structures, which is useful in a preliminary stage of the design process. However, when the structure does not extend indefinitely in the x and y directions, waveguiding effects need to be taken into account, and the model of the SWG will depend on the properties of the Bloch mode propagating through it. Accurate analysis of the SWG waveguide requires the use of advanced numerical tools optimized to analyze periodic structures [39–47]. Note that if there are several modes propagating through the SWG it generally cannot be modeled with a simple equivalent material.

SWG waveguides should not be confused with the periodically segmented waveguides proposed in the 1990s [53–55]. The main difference is that in segmented waveguides [53–55] the pitches are substantially larger than the wavelength, so these structures work in the radiation regime. Nevertheless, as they are designed to minimize the attenuation constant of the Bloch mode α_B and are

often implemented in low index contrast waveguides, propagation of guided light with low radiation losses can be achieved. It should be noted though that some concepts from segmented waveguides have been extended to mode conversion structures (tapers) for photonic crystals [56,57]. These tapers actually operate in the sub-wavelength regime.

3. Applications of crosswise SWGs

For the sake of clarity, the discussion on the applications of SWG structures is divided into two parts. This section is devoted to applications in which the propagation of light is crosswise to the SWG (along the x or y direction in Fig. 2). Propagation along the lengthwise direction (z axis in Fig. 2) is discussed in Section 4.

This section first re-visits Hertz's wire grid polarizer (section 3.1), and then discusses biology-inspired anti-reflective SWG coatings (Section 3.2). SWG patterned waveguides with controlled birefringence and for polarization rotation are presented in Section 3.3 and the concept of a SWG waveguide lens is presented in Section 3.4. In Section 3.5, fiber-chip grating couplers are extensively discussed, including SWG techniques for enhanced coupling efficiency, broadband operation, and polarization independence. An ultra-compact SWG-engineered wavelength demultiplexer is discussed in Section 3.6. A review of several applications of near-wavelength reflective structures, including state-of-the-art VCSELs, is presented in Section 3.7.

3.1. Hertz and the wire grid polarizer

Hertz's wire grid polarizer is a simple yet insightful example of the nature of sub-wavelength structures. The wavelength of the "electric beams" Hertz generated in his experiments was $\lambda \sim 33$ cm. The wire grid polarizer he used to study the polarization of these waves had a pitch of $\Lambda \sim 3$ cm, i.e. operating in the deep-sub-wavelength regime. The radio waves propagate crosswise through the grid lines, so that the device can be modeled using Rytov's formulas, i.e. Eq. (2) for polarization parallel to the grid and Eq. (3) for polarization perpendicular to the grid. Consider a the width of wires, n_1 the complex refractive index of the metal wires, and $n_2 = 1$ the refractive index of air. Since $|n_1^2| \gg |n_2^2|$, Rytov's formulas yield $n_{\parallel}^2 \approx \frac{a}{\Lambda} n_1^2$ and $n_{\perp}^2 \approx n_2^2 / (1 - \frac{a}{\Lambda})$ [8]. That is, for polarization parallel to the wires the grid behaves as a metal, blocking transmission. For polarization perpendicular to the wires the grid behaves as a dielectric, with no significant effect on transmission.

3.2. Sub-wavelength patterning of optical surfaces and waveguide facets

Arguably the first experimental observation of optical sub-wavelength structures dates back to the early 1960s.

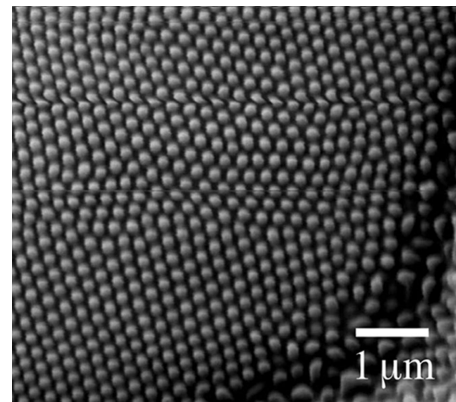


Figure 5 SEM micrograph of a moth eye. The pillars spaced at a sub-wavelength pitch reduce reflection from the surface of the eye, so that the insect is not easily detected by predators. Reproduced with permission from [58].

Bernhard and Miller [5], using scanning electron microscopy (SEM), discovered that the corneas of night-flying moth eyes were covered with an array of sub-wavelength spaced pillars, or "corneal nipples", as shown in Fig. 5. These structures reduce reflections from the eye, thereby reducing the risk that the insect be detected by its predators. This suggested the effectiveness of sub-wavelength structures in reducing reflections from surfaces, a principle that was first demonstrated by Clapham and Hutley a decade later [6].

The pillars of the moth-eye structure essentially act as a gradual refractive index transition between the incident medium and the surface, thereby providing index matching and suppressing Fresnel reflection [10, 28]. The basic design rules for such structures are: (i) spacing the pillars at a sub-wavelength pitch so that no diffraction takes place (see Section 2.1) and (ii) the height of the pillars should be of the order of $\lambda/2$ or larger in order to achieve a significant reduction in reflectivity. In the early 1980s surface SWGs with reflectivities as low as 0.035% at visible wavelengths were reported, and the intrinsic birefringence of these structures was exploited to produce half-wave and quarter-wave plates [11, 59, 60]. These results were extended to the silicon platform in [61]. A sub-wavelength patterned silicon surface with a reflectivity below 3% over the 200–1000 nm spectral band was reported in [62] for a grating with a pitch of $\Lambda = 150$ nm and a silicon height of $H = 350$ nm. An extensive review of optical elements with sub-wavelength patterned surfaces can be found in [63].

More recently, the use of sub-wavelength optical layers was proposed for modifying the properties of waveguides [64]. It is possible to control modal birefringence by depositing alternating layers of high- and low-index materials with a sub-wavelength pitch on top of a waveguide as shown in Fig. 6a. The rationale of this approach is as follows: for a mode traveling along the z direction, the sub-wavelength structure approximately acts as a homogeneous material of equivalent index n_{\parallel} or n_{\perp} for polarization parallel (quasi-TE) or perpendicular (quasi-TM) to the grating interfaces

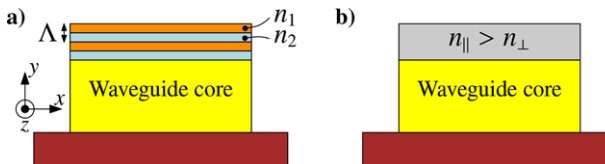


Figure 6 (a) Waveguide covered with a vertical sub-wavelength structure to control its birefringence. (b) The quasi-TE mode experiences a high equivalent index (n_{\parallel}) whereas the quasi-TM mode experiences a low equivalent index (n_{\perp}).

(Fig. 6b). Since n_{\parallel} and n_{\perp} can be tuned by changing the duty cycle and pitch of the SWG (see Eqs. (2) and (3)), the overall waveguide birefringence can be controlled. The effect on waveguide birefringence is so strong that only a few sub-wavelength layers may be sufficient to achieve optimal performance. Planar waveguide echelle grating demultiplexers were demonstrated with 48 channels and 256 channels, in which polarization effects due to waveguide birefringence were eliminated using a polarization compensator. The compensator consists of a triangular region in the slab waveguide section where the waveguide birefringence is modified by a high-index Si_3N_4 layer of sub-wavelength thickness. Using this technique, demultiplexer polarization-dependent wavelength shift was reduced to less than 10 pm [65]. The concept has also been exploited to design strongly birefringent waveguides, which significantly enhanced fabrication tolerances in an integrated polarization splitter, with a 20 dB polarization extinction ratio in the complete C-band [66].

Furthermore, waveguide facet reflectivity can be substantially reduced by etching “moth-eye” pillars into the waveguide end, as shown in Fig. 7, thereby obviating the need for anti-reflective coatings [67].

3.3. Sub-wavelength patterned waveguide cross-sections

The properties of waveguides can be dramatically changed by patterning one or several trenches in the waveguide cross-section. The slot waveguide shown in Fig. 8a uses

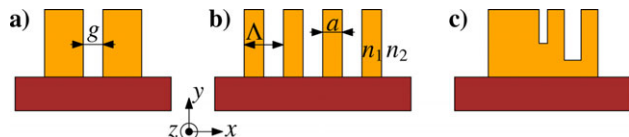


Figure 8 Cross-sections of (a) a slot waveguide, (b) a sub-wavelength multi-slotted waveguide designed to maximize birefringence, and (c) a sub-wavelength double-slot waveguide for polarization rotation. Waveguide mode propagation is along the z direction.

the large discontinuity of the electric field at silicon–trench interfaces to confine the light inside the low-index trench region [68, 69]. This effect has been used to maximize the modal field interaction with the surrounding material for sensing applications [70, 71]. The multi-slotted waveguide shown in Fig. 8b exploits the intrinsically large birefringence of transversal SWG trenches in combination with waveguide birefringence to achieve a group index birefringence (difference between the group indexes for TE and TM polarizations, $n_{g,\text{TE}} - n_{g,\text{TM}}$) of up to ~ 1.5 potentially enabling the implementation of compact polarization-selective delay elements for polarization handling applications [72]. Furthermore, by using asymmetric trenches, as in Fig. 8c, the mode polarization axes are rotated, so that with judicious design hybrid modes with $\pm 45^\circ$ polarization angle can be achieved. Using this structure a compact polarization rotator was demonstrated in silicon-on-insulator [73] and GaAs waveguides [74].

3.4. Waveguide lenses

In order to synthesize structures with a graded index profile it suffices to vary the duty cycle of the SWG, as shown in Fig. 9. The wide bars in the central region emulate a high refractive index, and the thinner bars synthesize a lower refractive index towards the edges. Such graded index structures were proposed and experimentally demonstrated with water waves [75] and polarized and unpolarized light in the 1990s [76–78]. In integrated optics these SWGs provide an interesting way to implement planar waveguide versions of free-space components. In this “free-space-optics-on-a-chip” configuration, light is confined vertically in the waveguide, but similar to free-space in the x - z plane (Fig. 9), with the propagation direction determined by the in-plane refractive index distribution $n(x, z)$. Planar waveguide gradient index (GRIN) lenses are a typical example of such structures [79–82]. GRIN lenses have been extensively used in free-space optics for focusing, collimation, and mode matching. The implementation of this concept in integrated optics alleviates some of the alignment problems compared to bulk optics components.

When light propagates along the z axis in the slab waveguide of Fig. 9 and the index distribution is quadratic along the x axis, focusing is achieved [80]. The quadratic distribution is given by $n(x) = n(x_0)[1 - (1/2)\rho(x - x_0)^2]$, where x_0 is the position of the optical axis and ρ is the

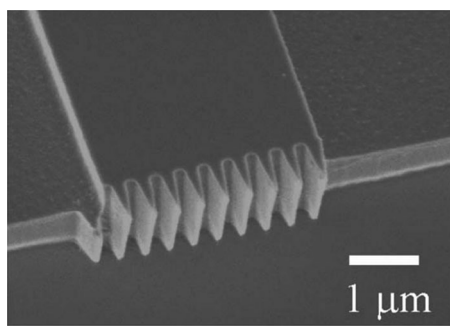


Figure 7 SEM micrograph of a silicon-on-insulator ridge waveguide facet patterned with a triangular SWG structure that acts as an anti-reflective coating. Reproduced with permission from [67].

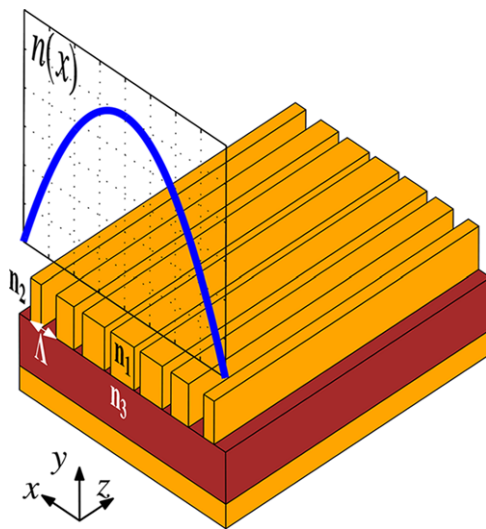


Figure 9 Schematic of a planar waveguide with a graded index realized by varying the duty cycle of the SWG. A quadratic refractive index distribution, $n(x)$, is synthesized along the x axis. Light propagation is along the z axis.

gradient coefficient. Light propagation along this quadratic structure can be described by Gaussian optics. The beam profile along the propagation direction can be determined using the ABCD law as follows [83]. The complex parameter q that describes the beam properties is defined as $1/q(z) = 1/R(z) - j\lambda/[\pi\omega^2(z)]$, with $\omega(z)$ the beam half-width and $R(z)$ the wave-front curvature radius. The beam parameters at the input (q_{in}) and output (q_{out}) of the system are then related through the ABCD parameters as $q_{\text{out}} = (Aq_{\text{in}} + B)/(Cq_{\text{in}} + D)$. The ABCD parameters describing quadratic media depend on the propagation length (L_{Prop}) and the square root of the gradient coefficient ($r = \sqrt{\rho}$):

$$\begin{bmatrix} A & B \\ C & D \end{bmatrix} = \begin{bmatrix} \cos(rL_{\text{Prop}}) & \sin(rL_{\text{Prop}})/r \\ -r \sin(rL_{\text{Prop}}) & \cos(rL_{\text{Prop}}) \end{bmatrix}. \quad (5)$$

By judiciously choosing the input beam width and gradient coefficient, lenses with beam focusing, defocusing, and collimating characteristics can be designed. The one-dimensional SWG shown in Fig. 9 provides a staircase approximation of the desired quadratic distribution. Alternatively, a two-dimensional array of circular nano-holes with a radius that varies along the x axis can be used [81]. The range of available indexes is determined by minimum feature size and vertical confinement constraints.

On-chip focusing has been experimentally demonstrated in the silicon-on-insulator platform using a one-dimensional SWG [80]. A conceptually similar structure has been used to experimentally demonstrate focusing of surface plasmon polaritons [82]. Light confinement in a quadratic medium can be achieved when the Gaussian beam diffraction and GRIN focusing effects compensate each other. This configuration has been theoretically discussed

for one-dimensional and two-dimensional sub-wavelength structures [79, 81].

The free-space-optics-on-a-chip concept has also been applied to shape light propagation in the silicon platform [84]. In this case, lens-like conformal transformation of light propagation in the slab plane is implemented by means of a two-dimensional sub-wavelength hole lattice, where the hole distribution is engineered to obtain the desired index profile. Low-loss propagation was experimentally demonstrated in the wavelength range $1.4\text{--}1.8\ \mu\text{m}$. Waveguide lenses with sub-wavelength lattices have been studied by several groups [85, 86].

3.5. Fiber-chip grating couplers

The cross-sectional area of nanophotonic waveguides is more than two orders of magnitude smaller than that of a standard single-mode fiber, making efficient light coupling between both elements challenging. A widely used coupling solution are surface grating couplers [23, 52], which extract light from the planar waveguide and radiate it upwards and downwards. By situating an optical fiber above the chip, part of the radiated light is captured. Grating couplers are defined lithographically, so that they can be placed anywhere on the chip surface, thereby enabling wafer-scale testing, which is particularly useful for large-volume fabrication. An alternative coupling solution based on SWG waveguide facet couplers is discussed in Section 4.2.

This section is devoted to the use of crosswise SWG structures in surface grating couplers to simplify their fabrication and enhance their performance. First, some grating coupler fundamentals are introduced (Section 3.5.1). SWG techniques that improve coupling efficiency (Section 3.5.2), bandwidth (Section 3.5.3), and polarization dependence (Section 3.5.4) and enable mid-infrared operation (Section 3.5.5) are then described. An overview of the SWG designs that reviewed here can be found in Table 1.

3.5.1. Surface grating coupler fundamentals

Figure 10a shows a schematic side view of a surface grating coupler, with the waveguide mode traveling in the z direction in an input waveguide with core refractive index n_{Si} . For the silicon wire waveguides considered in this discussion, the silicon thickness H_{Si} is typically in the range 220–400 nm. As the mode encounters segments with different indexes n_i , it partially diffracts its power upwards with an angle θ_k . If the grating parameters are constant, i.e. $\Lambda_{z,i} = \Lambda_z$, $a_{z,i} = a_z$, and $n_i = n_1$, the radiation angle is given by the grating equation [23]:

$$n_d \sin \theta_k = n_B + k\lambda/\Lambda, \quad (6)$$

where n_d is the refractive index of the cladding material (see Fig. 10). Since the fiber–chip grating couplers extract light from the waveguide over a comparatively short length

Table 1 Overview of SWG-based grating coupler designs. CE, coupling efficiency; BW, 3 dB bandwidth.

Ref.	Year	CE (dB)	BW (nm)	Remarks
[16]	2009	-3	-	TM pol.; simulated
[87]	2009	-4.7	40	DUV fabrication
[88]	2010	-3.8	60	
[89]	2010	-4.2	60	TM pol.
[89]	2010	-3.7	55	TM pol.; apodized
[90]	2011	-1.7	-	blazed; simulated
[91]	2011	-4.5	60	pol. independent; simulated
[92]	2012	-5	55	TM pol.; DUV fabrication
[93]	2012	-4.1	57	silicon membrane on glass
[94]	2012	-2.4	60	optimized H_{box}
[95]	2012	-5.6	100	reduced index
[96]	2012	-3.5	80	reduced index
[97]	2012	-2.8	300	trapezoidal SWG; simulated
[96]	2012	-5.5	-	mid-infrared; suspended waveguide
[98]	2012	-5	-	mid-infrared; silicon-on-sapphire
[99]	2012	-3	50	apodized; focusing; TM pol.
[100]	2013	-5.1	115	reduced index and SWG pitch
[101]	2013	-1.8	60	apodized and optimized H_{box}
[102]	2014	-6.5	-	polarization independent

of the order of $10 \mu\text{m}$, they generally introduce a strong perturbation in the waveguide. Consequently, in Eq. (6) instead of using the effective index of the unperturbed wave-

uide mode, the Floquet mode index (n_B) is used [23]. Note that only the diffraction orders for which $\sin \theta_k$ is real, i.e. $|n_B + k\lambda/\Lambda_z| < n_d$, radiate power from the waveguide [23]. The pitch of the grating, Λ_z , is often designed so that only the order $k = -1$ propagates [52]; see though [103] for a notable exception operating with $k = -2$. As discussed in Section 2.2, an accurate calculation of the Bloch mode effective index, n_B , generally requires specific numerical tools [39–47]. The cladding material is usually air ($n_d = 1$), silicon dioxide, or an index-matching liquid ($n_d \sim 1.45$).

The width of the grating coupler in the x direction is designed to match the size of the fiber core, resulting in a typical grating width $W_{\text{gr}} = 10\text{--}15 \mu\text{m}$. To obtain a low-loss transition with single-mode interconnecting waveguides adiabatic tapers are used. Alternatively, the whole grating can be curved following parabolas to focus light directly on the waveguide [104, 105].

3.5.2. Coupling efficiency

The fraction of power that couples from the waveguide mode to the optical fiber mode (or vice versa) mainly depends on three factors:

- Grating directionality, i.e. the fraction of waveguide power p_{up} that diffracts towards the fiber (the power that escapes into the substrate is lost).
- The overlap integral, p_{ol} , between the radiated beam and the near-Gaussian optical fiber mode [52]: $p_{\text{ol}} = |\int e_f e_r^* dz'|^2$ (see Fig. 10a). Note that the overlap integral has to be carried out over the complex fields so that phase information is taken into account.

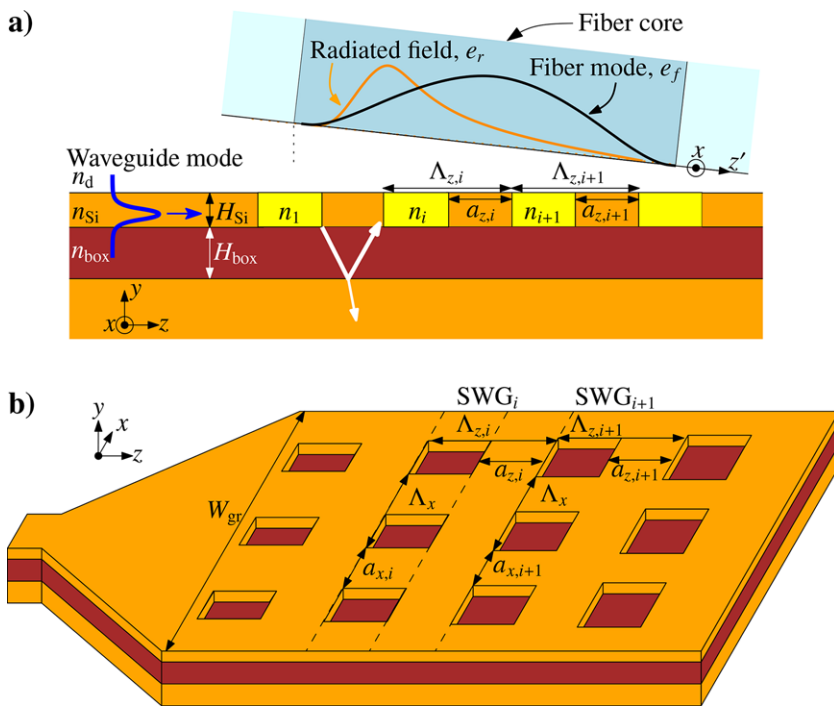


Figure 10 (a) Two-dimensional model of a fiber-chip grating coupler. Light traveling along the z axis in the waveguide mode is scattered upwards and downwards by a diffractive grating. A fiber situated above the grating captures a fraction of the diffracted light. (b) Sub-wavelength (non-diffractive) structures along the x direction are used to control the equivalent refractive index in the grating trenches, thereby controlling the strength of the grating and enhancing coupling efficiency.

- The amount of power, r , that is reflected back from the grating into the waveguide.

The overall coupling efficiency can then be estimated as $\eta = (1 - r)p_{\text{up}}p_{\text{ol}}$.

Grating directionality can generally be enhanced in two ways. The first is by optimizing the buffer layer (SiO_2 bottom oxide, or “box”) thickness, H_{box} , so that the beam that is radiated downwards, upon reflection at the box–substrate interface (see Fig. 10a), interferes constructively with the beam that is radiated upwards. In practice, commercial silicon-on-insulator wafers only provide a discrete set of box thicknesses, from which the best alternative has to be chosen. By increasing the reflectivity of the box–substrate interface, for instance by selectively removing the substrate and depositing a metal layer, directionality can be further enhanced [106–108]. The second technique to increase the fraction of power radiated upwards is to mitigate downwards radiation. This can be achieved either by blazing the grating, i.e. using triangular or trapezoidal teeth (instead of the conventional rectangular form) [109, 110], or by optimizing the thickness of the silicon layer, H_{Si} [111, 112]. An implementation of a blazed grating coupler using a SWG structure is proposed in [90], with a simulated coupling efficiency of -1.7 dB .

The overlap integral of the radiated field with the fiber mode (p_{ol}) is determined by the fraction of waveguide power that is radiated in each grating period, i.e. the strength of the grating. This fraction is approximately proportional to the refractive index difference between the teeth of the grating (n_{Si}) and the grooves (n_i). If the grating grooves are fully etched, i.e. $n_i = n_d$, the index contrast is large (~ 2), resulting in a strong grating with a narrow radiated beam that produces an overlap of only $p_{\text{ol}} \sim 0.35$ with the SMF-28 fiber mode [16]. Consequently, conventional grating couplers use a tightly controlled shallow etch in the grating region [52], thereby reducing the grating strength and enhancing the field overlap. However, the addition of this shallow etch step to the full etch required to define the waveguides adds complexity to the fabrication process. Additionally, as long as the same fraction of power is radiated in every period, the radiated near-field always has an exponential shape, with a maximum possible overlap of $p_{\text{ol}} = 0.8$ with the near-Gaussian fiber mode [23]. In order to increase the field overlap beyond this point, an apodized grating design is required, in which the strength is varied along the structure to obtain a radiated beam that resembles the optical fiber mode.

SWG structures enable the design of efficient apodized grating couplers that can be fabricated in a single, full etch step. Consider the SWG-structured grating shown in Fig. 10b. Along the z direction the device acts a conventional (diffractive) grating. The periodic structures along the x direction (labeled as SWG_i) have a sub-wavelength period and thus act as artificial homogeneous media, synthesizing the equivalent indexes n_i in the grating grooves. While these refractive indexes can be approximately estimated by Rytov formulas (2) and (3), their exact values can be obtained by treating each SWG as a two-dimensional

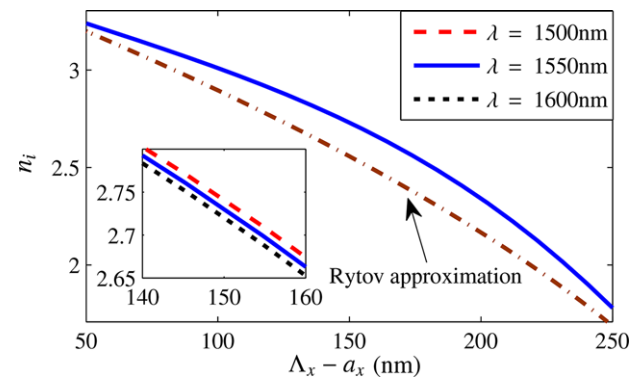


Figure 11 Equivalent index of a SWG multilayer slab with pitch $\Delta_x = 300 \text{ nm}$ as a function of hole size ($\Delta_x - a_x$), computed with a two-dimensional mode solver. The index value given by the zero-order Rytov approximation is shown for comparison. The inset shows that the equivalent index varies only slightly with wavelength. TM polarization (electric field along the y axis) is assumed.

multilayer slab, and computing the effective index of its fundamental mode [16]. By changing the size a_x of the silicon segments of the SWG the equivalent index can be controlled, yielding a range of values n_i as shown in Fig. 11. Designing a uniform coupler is then straightforward: (i) through simulation of the grating structure in Fig. 10a the value of n_i that yields the highest coupling efficiency is determined; this results in $n_i \sim 2.7$ and (ii) using the data in Fig. 11 as a look-up table the physical dimensions of the SWG structure that yields the desired value of n_i are obtained. Using this approach a fully etched grating with a coupling efficiency around $\eta = -4 \text{ dB}$, which compares favorably to dual-etch gratings, was obtained [88, 89]. Similar results are achieved when the structure is mass-fabricated with deep-ultraviolet (DUV) lithography [87, 92]. By furthermore optimizing the buffer thickness to $H_{\text{box}} = 1 \mu\text{m}$ a coupling efficiency of -2.4 dB was reported in [94]. An implementation in a silicon membrane on a glass substrate with a coupling efficiency of -4.1 dB is described in [93].

Furthermore, using SWG structures a grating can be apodized by simply varying the SWG duty cycle ($a_{x,i}/\Delta_x$) along the grating (see Fig. 10b). In [89] it was found that a linearly decreasing variation of the indexes n_i from $n_1 = 3.3$ to $n_{17} = 2$ yields an almost perfect overlap with the optical fiber mode ($p_{\text{ol}} = 0.94$). However, the decreasing values of n_i also result in a reduction of the effective index of the Bloch mode $n_{B,i}$ in each grating period. From Eq. (6) this in turn results in a variation of the radiation angle θ_{-1} along the grating, which, if left uncompensated, would result in a dramatic reduction in coupling efficiency. This penalty can be avoided by chirping the grating, that is, changing the pitch $\Delta_{z,i}$ along the grating so that the quantity $n_{B,i} - \lambda/\Delta_{z,i}$ remains constant. This ensures that all grating elements radiate with the same angle and the phase of the radiated field is linear in the grating region. Figure 12 shows a SEM image of such an apodized grating which exhibits a coupling efficiency of -3.7 dB

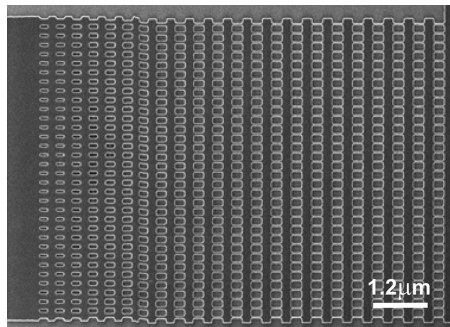


Figure 12 SEM image of an apodized fiber-chip grating coupler using fully etched SWG trenches. The apodization gradually decreases the equivalent index in the trenches, producing a Gaussian-like radiated beam that matches the fiber mode.

[89]. In [99] an apodized design with focusing and a coupling efficiency of -3 dB was presented. Using a triangular array of circular holes, apodization, and an optimized buffer thickness an efficiency of -1.8 dB was achieved in [101]. It is noteworthy that efficient grating apodization also reduces back-reflections from the grating coupler, since the refractive index discontinuities are smoothed.

3.5.3. Spectral bandwidth

Grating couplers exhibit a limited bandwidth. From the grating equation (6) it is apparent that the radiation angle θ_{-1} changes with wavelength. In fact, for large angular variations comparable to the numerical aperture of the fiber (which has to be kept at a fixed angle over the grating) coupling to the fiber is dramatically reduced. Let $\Delta\theta_{-1}$ be the angular variation that produces the maximum acceptable coupling efficiency penalty, and let $\Delta\lambda$ be the change in operation wavelength that causes this variation $\Delta\theta_{-1}$. Then $\Delta\lambda$ is directly proportional to the bandwidth of the grating coupler. Since $\Delta\theta_{-1} = \frac{d\theta_{-1}}{d\lambda}\Delta\lambda$, it is found that $\Delta\lambda = \frac{d\lambda}{d\theta_{-1}}\Delta\theta_{-1}$, that is, the bandwidth of the coupler is proportional to $\frac{d\lambda}{d\theta_{-1}}$. In [95] it is shown that if the nominal radiation angle (θ_{-1}) and the cladding refractive index of the structure (n_d) are fixed, the bandwidth of the coupler is approximately proportional to $1/n_B$. The derivation is as follows. From the grating equation (6) it is found that $\frac{d\lambda}{d\theta_{-1}} = \Lambda \frac{d}{d\theta_{-1}}(n_B - n_d \sin \theta_{-1})$. Taking into account that $n_B = n_B(\lambda)$, that λ depends on θ_{-1} , ignoring the wavelength dependence of n_d , and applying the chain rule, the following equation is obtained:

$$\frac{d\lambda}{d\theta_{-1}} = \left| \frac{n_d \cos \theta_{-1}}{\frac{1}{\Lambda} - \frac{dn_B}{d\lambda}} \right| \quad (7)$$

In the radiation regime $dn_B/d\lambda$ is negative (see Fig. 3b), so that the two terms in the denominator actually add. Thus, for improved bandwidth, the absolute values of $1/\Lambda$ and $dn_B/d\lambda$ have to be minimized. From Eq. (6), $1/\Lambda$ is

proportional to n_B . Furthermore, it can be assumed that $dn_B/d\lambda$ is also proportional to n_B , because as n_B decreases, light is more loosely guided and dispersion diminishes. Thus, by decreasing n_B both factors are reduced, and grating bandwidth is enhanced.

Reducing n_B in turn requires lower refractive indexes in the grating, which can be obtained by using alternating layers of air and SWG structures, instead of the conventional structure of alternating layers of silicon and SWG structures. A bandwidth of ~ 100 nm with a coupling efficiency of -5.6 dB was obtained in [95]. A focusing grating coupler with a similar structure was reported in [96] for which the bandwidth is ~ 80 nm with peak coupling efficiency of $\eta = -3.5$ dB. The SWG structure itself is only slightly dispersive (see inset in Fig. 11). However, in bandwidth-optimized couplers this effect is noticeable so that by reducing the dispersion of the SWG, by simply decreasing its pitch, a further bandwidth improvement of up to 115 nm can be achieved [100]. Finally, in [97] trapezoidal SWG holes are used, which not only provide a lowered effective index but also produce a blazing effect. In combination with an optimized buffer thickness this structure exhibits a simulated bandwidth of ~ 300 nm and a coupling efficiency of -2.8 dB.

3.5.4. Polarization dependence

Grating couplers are effective polarization filters, because the index of the Bloch mode in the grating region, n_B , is highly birefringent, resulting in largely different radiation angles for TE and TM polarization. For applications in which the input polarization state cannot be controlled this poses a serious limitation, which is usually addressed with two-dimensional grating couplers [113]. Consisting essentially of two grating couplers quasi-perpendicularly interleaved with each other, these devices couple the two orthogonal fiber polarization states into the TE polarization of two perpendicular waveguides. Gratings that couple the orthogonal fiber polarizations into the quasi-TE and quasi-TM modes of the same waveguide, but traveling in opposite directions, have also been reported [114]. In thick silicon-on-insulator waveguides ($H_{Si} > 1 \mu m$), where the Bloch mode birefringence is considerably smaller, polarization-independent gratings that couple the orthogonal fiber polarization states into the TE and TM states of the same waveguide, traveling in the same direction, can be designed [115].

The intrinsically high birefringence of SWG structures can be exploited to obtain polarization-independent grating couplers for silicon wire waveguides [91]. The rationale for this is as follows. Consider the grating structure of Fig. 10b. In the silicon (non-SWG) slab regions, the effective index of the TE (x -polarized) mode will be larger than the effective index of the TM (y -polarized) mode. However, in the SWG regions, the effective index of the TE mode is given approximately by n_{\perp} , which is smaller than the effective index of the TM mode given by n_{\parallel} (see Eqs. (2) and (3)). If the grating region is designed so that these two effects cancel each other, the effective index of the Bloch mode

will be identical for both polarizations, and, consequently, the grating becomes polarization independent. Using this approach a simulated coupling efficiency of -4.5 dB for both polarizations with a 60 nm bandwidth is reported in [91]. An experimental demonstration of this structure, with a polarization-insensitive coupling efficiency of -6.5 dB, is described in [102].

3.5.5. Mid-infrared operation

The mid-infrared wavelength range holds a strong potential for nonlinear phenomena and spectroscopic sensing in silicon waveguides [116]. SWG couplers have already been shown to offer interesting coupling solutions at $\lambda = 2.75$ μm , both in suspended waveguides [96] and in silicon-on-sapphire [98], with coupling efficiencies around -5 dB. It is noteworthy that at these wavelengths the minimum pitch required for sub-wavelength operation is considerably larger, which facilitates device fabrication.

3.6. Wavelength multiplexers

As discussed in the previous section, the combination of diffractive gratings and SWGs can provide a variety of solutions for efficient fiber–chip coupling. In this section the design of compact, high-performance wavelength multiplexers using the same combination is described.

In a sidewall grating demultiplexer, shown in Fig. 13a and b, the dispersive element is the grating etched in the sidewall of the input waveguide, where light is preferentially diffracted by grating teeth blazed for the +1 order. This device was originally modeled analytically with each tooth acting as a Huygens wavelet source and was confirmed with two-dimensional finite-difference time-domain simulations [117]. For efficient coupling to the output receiver waveguides, the field distribution at the focal curve (Rowland circle) must match the mode profile of the receiver waveguide. A Gaussian near-field distribution is required to ensure the far-field matching condition at the focal curve. Grating apodization is used to ensure a Gaussian diffracted near-field profile. The grating is chirped to achieve a flat phase front along the entire length of the apodized grating. Fundamental to the operation of the sidewall grating multiplexer is a sub-wavelength nanostructure between the sidewall grating waveguide and the slab waveguide of the combiner region. Such a nanostructure acts as a lateral cladding to ensure the channel waveguide with the sidewall grating supports a fundamental guided mode, while simultaneously providing waveguiding for the light diffracted in the direction normal to the channel waveguide. At the same time, the SWG is gradually transformed to a slab waveguide using a triangular (moth-eye-like) index-matching transition. This results in efficient coupling of the diffracted light to the slab waveguide as evident by a remarkable 4 dB loss reduction [118]. The total intrinsic device loss, which includes diffraction loss, coupling loss from the waveguide grating to the slab waveguide, and excess loss due to the field mismatch at the receiver

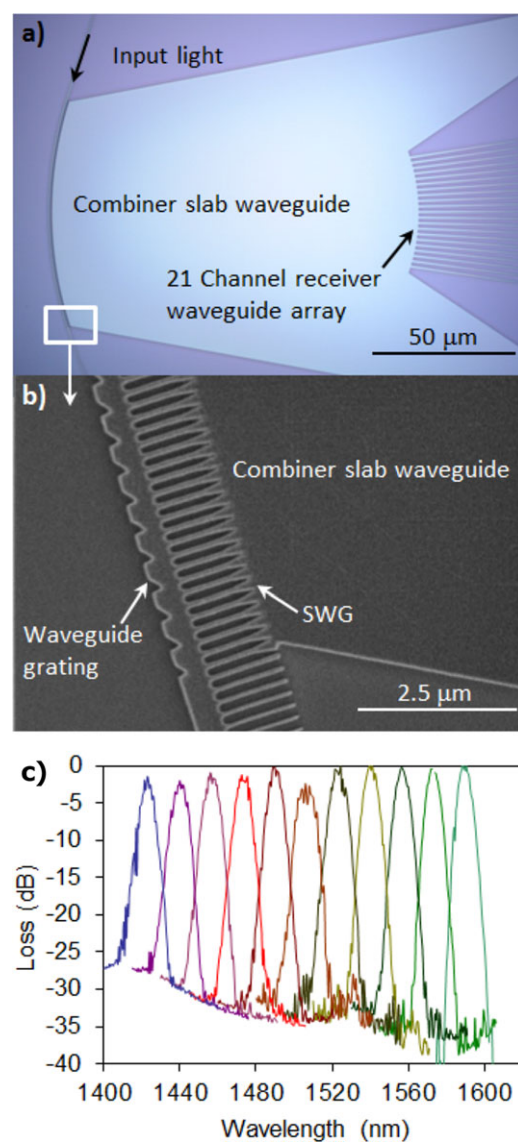


Figure 13 (a) Optical image of a sidewall grating demultiplexer showing the input waveguide and the 21-channel output receiver waveguide array. (b) SEM image of the input waveguide with blazed sidewall grating and SWG region between the input waveguide and the slab waveguide combiner. (c) Demultiplexed spectra for a wavelength range of 1340 to 1620 nm (TE polarization, double-pass configuration).

waveguide, was measured to be 3–4 dB [118]. Some reduction in performance at shorter wavelengths (Fig. 13c) is attributed to approaching the bandgap of the SWG fiber–chip coupler.

At the same time, the SWG is gradually transformed to a slab waveguide using a triangular (moth-eye-like) index-matching transition region. This results in efficient coupling of diffracted light to the slab waveguide. The complete device has a compact footprint of $100 \times 160 \mu\text{m}^2$ [118]. The measured transmission spectra in Fig. 13c show an operation bandwidth of 300 nm (1340–1640 nm) and crosstalk of 25–35 dB in a double-pass configuration.

3.7. Near-wavelength structures

As discussed in Section 2.1, periodically structured waveguides with a near-wavelength pitch that only support reflected and transmitted zero-order diffraction can produce strong and wideband reflections for normally incident light (i.e. propagation along the x direction in Fig. 2). For high-refractive-index contrasts, these structures, although working in the non-diffractive regime, can exhibit a rich behavior which cannot be explained in terms of the simple Fabry–Perot resonances predicted by the effective medium theory. Two different interpretations of near-wavelength high-contrast gratings are found in the literature. The first one makes use of the Bloch modes propagating in the z direction along the periodic waveguide [119, 120]. The second one relies on the waveguide array modes propagating in the x direction along the array of slabs that constitute the grating [36, 121, 122]. In the framework of the latter, it is observed that for the effective medium theory to be applicable a single waveguide array mode should propagate in the grating region. In this case, vertical bouncing of the mode inside the grating region gives rise to simple Fabry–Perot resonances. On the other hand, if more than one mode exists in the grating region the model becomes increasingly complex because modes couple at the grating interface giving rise to a much richer and less intuitive behavior. Near-wavelength high-contrast gratings such as those achievable with silicon or InP–air interface do fulfill the multimode condition and thus exhibit a rich behavior which has been studied for filtering purposes since the early 1990s [123]. First realizations of such filters were used in the reflection regime [124] and were later extended to the transmission regime [125]. Advanced design strategies to engineer the spectral response of such devices have been established in [119, 120]. Other interesting applications of SWGs with near-wavelength pitch include a mirror used to improve grating coupler performance [126], high-speed beam steering [127], polarization management [128–130], highly reflecting mirrors [38, 131], and focusing lenses [132, 133].

However, one of the most relevant applications of these structures probably is their use in VCSELs. These devices have become the dominant optical source for multimode fiber-based local area networks at $\lambda = 850$ nm, and efforts are ongoing to develop low-cost long-wavelength VCSELs emitting in the 1.3 and 1.5 μm bands. One of the techniques proposed to make cost-effective long-wavelength VCSELs is to use a SWG structure on top of the device acting as a highly reflective mirror, substituting the top DBR in a conventional VCSEL. This type of SWG, consisting of high-refractive-index bars surrounded by low-index materials, is known as a HCG or photonic crystal membrane (PCM) and can be designed for high reflectivity and broad bandwidth operation. A theoretical analysis of a VCSEL in which vertical confinement was obtained through a PCM is presented in [37]. The PCM mirror consisted of indium phosphide rods embedded in air and its parameters (pitch, duty cycle, and membrane thickness) were optimized to obtain a peak reflectivity in excess of 97% for an 80 nm bandwidth; the complete laser structure was then simulated confirming the

viability of the idea. The first reported HCG comprised a one-dimensional periodic structure of silicon bars on silicon dioxide with an air cover [38]. Simulation results obtained by rigorous coupled wave analysis showed the potential application of these structures to get high-reflectivity mirrors ($R > 99\%$) for fractional bandwidths greater than 30%. Applications of HCGs to VCSELs appeared soon after. In [17] an 850 nm HCG AlGaAs VCSEL was reported, and in [134, 135] the HCG mirror was implemented as a microelectromechanical system membrane allowing VCSEL tunability in a 20 nm range. Several advantages can be obtained by implementing a HCG mirror in a VCSEL [136]: (i) it provides polarization discrimination and thus avoids mode jumping between orthogonal polarizations, (ii) the angular discrimination (incidence angle-dependent reflectivity) allows for increased device area and power without exciting spurious lateral modes, and (iii) due to the small size and mass of HCG membranes compared to conventional DBRs they enable fast wavelength tuning [137].

The broadband nature of HCG mirrors and the intrinsic wavelength scalability make these structures highly tolerant to fabrication errors [138]. Several authors have studied the fabrication tolerances of HCG mirrors. In [139] the authors studied the tolerances of the mirror reflectivity of an InGaAs/GaAs 980 nm VCSEL as a function of imperfections in the width and absorption of the HCG stripes. It was found that HCG reflectivity is rather robust and tolerant to these imperfections. In fact it was shown that for width variations of ~ 35 nm the reflectivity still exceeds 99% and that losses due to free carrier absorption or surface defects caused negligible reflectance penalty.

While in most cases the role of the near-wavelength structure inside a VCSEL is to substitute one of the vertical mirrors, these structures can also be used for light confinement in the lateral dimension. In [140] an optically pumped CMOS compatible laser structure was reported. The active III–V layer is sandwiched by wafer bonding between silicon dioxide layers in which a PCM structure is defined. The structure not only acts as a mirror in the vertical dimension but, by laterally changing its geometric parameters, it also enables lateral confinement of the fields.

4. Applications of lengthwise SWGs

This section is devoted to lengthwise SWGs, that is, sub-wavelength structures in which light propagates perpendicularly to the interfaces of the structure (along the z direction in Fig. 2). The need to consider Bloch–Floquet mode propagation makes lengthwise SWG structures intrinsically more complex than their crosswise counterparts. Yet, some of the most interesting features and applications of SWGs arise precisely from this complexity. This section starts with a discussion of SWG waveguides and ultra-low-loss crossings (Section 4.1). Mode converters between SWG waveguides and conventional waveguides or optical fibers are presented in Section 4.2. Fourier transform spectrometer chips, all-optical switches, and high-speed modulators are described in Sections 4.3, 4.4,

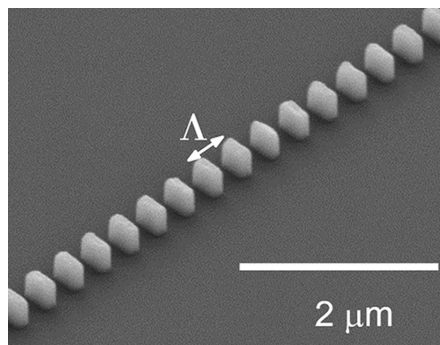


Figure 14 SEM image of a SWG waveguide having a width of 300 nm, a pitch of 300 nm, and a duty cycle of 33%. Propagation losses were measured to be ~ 3.0 dB/cm at $\lambda = 1.5 \mu\text{m}$.

and 4.5, respectively. Section 4.6 is dedicated to high-performance and compact MMI couplers. Finally, the possibilities of dispersion engineering with SWGs are discussed, yielding integrated couplers with bandwidths exceeding 400 nm (section 4.7).

4.1. Sub-wavelength waveguides and crossings

As outlined in Section 2.2 a SWG dielectric waveguide comprises a core composite medium formed by periodically interlacing two or more optically transparent materials at a sub-wavelength scale. By modifying the pitch, width, or duty cycle of the SWG, the effective refractive index of the waveguide core can be controlled.

While periodic waveguides have been extensively investigated for several decades, efforts have almost exclusively focused on photonic crystals with a pitch $\Lambda \sim \lambda/(2n_B)$ that creates a bandgap at the operational wavelength range, as opposed to the $\Lambda < \lambda/(2n_B)$ pitch for SWG waveguides. In photonic crystal structures, a waveguide is typically created by introducing a line defect in the periodic lattice that creates defect states localized within the lattice photonic bandgap [141]. If the operating wavelength is within the photonic bandgap of this lattice, waveguiding can occur due to the mirror-like effect of the lattice, confining the light laterally. If the operating wavelength is outside the photonic bandgap, index guiding can arise when the lateral cladding effective index is lowered by the perforations. While SWG waveguides belong to a sub-category of photonic crystal waveguides, they operate in the linear dispersion region, outside the photonic bandgap, and require no lateral photonic crystal lattice. The fundamental waveguiding mechanism is the propagation of Bloch–Floquet mode of the SWG structure. Waveguides comprising periodic dielectric rods (without a lateral photonic crystal lattice cladding) were first theoretically considered in [39, 142, 143].

SWG waveguides with silicon segments spaced at a sub-wavelength pitch, $\Lambda < \lambda/(2n_B)$, were experimentally demonstrated in [144]. These SWG waveguides, shown in Fig. 14, have the following properties: a width of 300 nm, a pitch of 300 nm, a duty cycle of 33%, and waveguide

propagation losses ~ 3.0 dB/cm at $\lambda = 1.5 \mu\text{m}$ for quasi-TE and for quasi-TM polarization. These propagation losses are comparable to those of conventional silicon-wire waveguides, indicating that the sub-wavelength patterning introduces virtually no additional losses. While this is expected from the theoretical discussion on sub-wavelength Bloch mode propagation in Section 2.2, it is remarkable considering that along a 1 cm propagation distance, the light in this waveguide passes through over 33,000 high- and low-refractive-index interfaces with an index contrast of $\Delta n \sim 1.9$. A subsequent rigorous theoretical study indeed confirmed that this SWG waveguide is theoretically lossless in the absence of fabrication imperfections [145], and Bloch mode orthogonality was used to derive closed-form expressions for the scattering coefficient at the interface between periodic segments.

Temperature-independent (athermal) sub-wavelength waveguides were also reported [146, 147], using a combination of SU-8 polymer and silicon materials. Since SU-8 has a negative thermo-optic coefficient while in silicon this coefficient is positive, a waveguide created by interleaving specific amounts of these two materials can be made athermal by design. In [146] it was shown through interferometric measurements that for a duty cycle of 66% the SWG waveguide exhibited negligible temperature dependence for TE polarization over a 7 °C temperature range. However, for TM polarization comparatively large duty cycles were required for athermal operation yielding very small feature sizes of the order of 50 nm. To increase the minimum feature size, SWG waveguides with bridging segments were proposed in [147]. Figure 15 shows SEM images of the fabricated bridged SWG waveguides. The bridging segments provide an extra degree of freedom in designing athermal SWG waveguides. Athermal operation was experimentally demonstrated with minimum feature sizes above 100 nm for both TE and TM polarization [147].

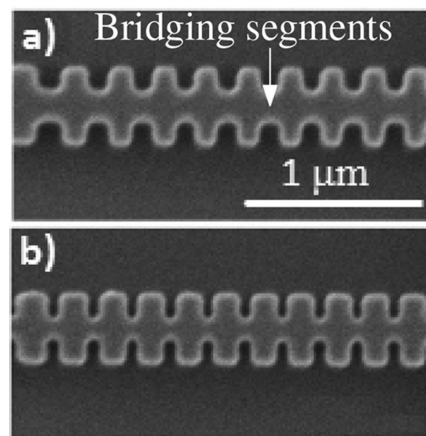


Figure 15 SEM images of bridged SWG waveguides with a width of 450 nm, a pitch of 250 nm, and a duty cycle of (a) 50% and (b) 65%. By cladding the waveguides with a polymer that has a thermo-optic coefficient opposite to that of the core material (silicon), athermal operation is achieved. Reproduced with permission from [147].

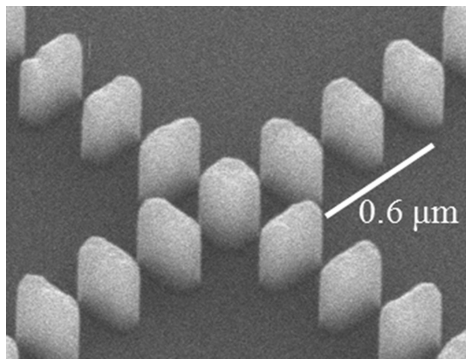


Figure 16 SEM image of a SWG waveguide crossing with segments with a width of 300 nm, a pitch of 300 nm, and a duty cycle of 33%. Central segment dimensions are 220 nm × 220 nm. The sub-wavelength patterning delocalizes the waveguide mode, reducing scattering at intersection and yielding measured per crossing losses of ~ 0.02 dB.

A further advantage of SWG waveguides is their intrinsic ability to intersect each other, facilitating circuit interconnectivity and routing. When a conventional waveguide intersects another, it creates a region with no lateral confinement resulting in coupling to radiation modes (loss) and coupling to the intersecting waveguide (crosstalk). However, when two SWG waveguides intersect each other, both crossing loss and crosstalk can be minimized for the propagating Bloch–Floquet mode [18]. The main reason why SWG waveguides can form efficient crossings is that the propagating Bloch–Floquet mode is delocalized in the crossing region, i.e. the mode expands and the modal field overlap with the intersecting waveguide (acting as a scattering center) is reduced. Since the effective index of the intersecting waveguide is also reduced (compared to a conventional waveguide), the scattering strength at the intersection decreases. Crossings have also been implemented using inverse tapers to effectively push the mode up over the intersecting waveguide confining the light in the upper layer [148, 149]. However, the fabrication of these structures is more complex and requires multiple etch steps. Crossings based on periodic Bloch mode excitation from periodically spaced intersecting waveguides have been demonstrated but require multiple crossings to operate [150, 151]. Photonic crystal waveguide crossings have also been proposed [152], but require small feature size and high fabrication accuracy. SWG waveguide crossings only require a single etch step and are robust to fabricate. In addition, the ability to control the SWG properties, particularly grating duty cycle, allows for an additional degree of freedom in crossing design.

Figure 16 shows a SEM image of a fabricated SWG waveguide crossing. At the point of intersection a square segment is used to ensure optical symmetry. Experimental results confirmed a low loss per crossing of 0.02 and 0.04 dB for TE and TM polarizations and a crosstalk below -40 dB at $\lambda = 1.55 \mu\text{m}$ [18]. Sub-wavelength waveguide crossings have also been implemented as cascaded MMI couplers, where SWGs were used to reduce the insertion loss. A 101×101 MMI crossing matrix was fabricated with a pitch

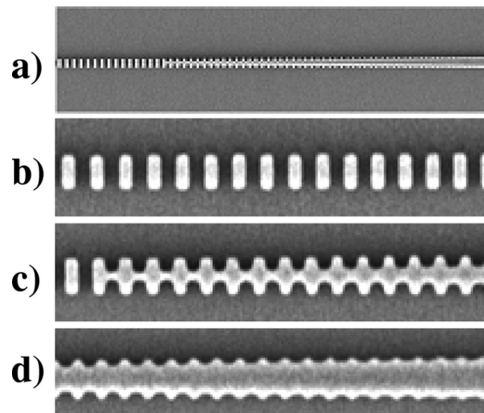


Figure 17 SEM images of a SWG mode converter for fiber-to-chip facet coupling with ~ 1 dB efficiency. (a) The overall structure. (b) SWG waveguide segment. (c) Transition region from SWG waveguide to conventional waveguide. (d) Coupler structure at the junction with the conventional strip waveguide region.

of $3.08 \mu\text{m}$ to ensure near-lossless Bloch mode propagation [153]. Loss per crossing was measured as ~ 0.02 dB, with a crosstalk below -40 dB at $\lambda = 1.55 \mu\text{m}$.

4.2. SWG mode converters

In order to exploit the flexibility afforded by SWG waveguides, they need to be integrated and interconnected with conventional waveguides. This requires adiabatically converting the SWG waveguide Bloch–Floquet mode to the fundamental mode of the conventional waveguide. Figure 17 shows the structure that is used to perform this mode conversion: the SWG on the left-hand side of Fig. 17a is gradually transformed into the conventional waveguide (right-hand side of 17d) by chirping the grating pitch and duty cycle and incorporating bridging elements between the waveguide segments [15, 154]. While the mode delocalization effect in these transitions is similar to inverse tapers [155], they must be carefully designed to suppress back-reflections by avoiding Bragg-reflection zones that can form locally along the device [156].

This concept of a SWG mode converter was first used as a fiber–chip edge coupler, since the delocalized mode of the SWG waveguide can be designed to be close in size, shape, and effective index to that of a single-mode fiber [154]. This fiber–chip edge coupler is robust and tolerant to fabrication variations, with only -0.1 dB coupling loss penalty for a 50 nm tip width change. The nominal tip width is 350 nm, which is about three times larger than the conventional inverse taper width (~ 100 nm). The intrinsic loss of the SWG mode converter was determined in an independent measurement on a series of back-to-back mode converters (up to 60) as -0.23 dB for TE polarization and -0.47 dB for TM polarization [18]. The total fiber–chip coupling efficiency was reported as a remarkable -0.9 dB for TE polarization and -1.2 dB for TM polarization [15]. A subsequent theoretical

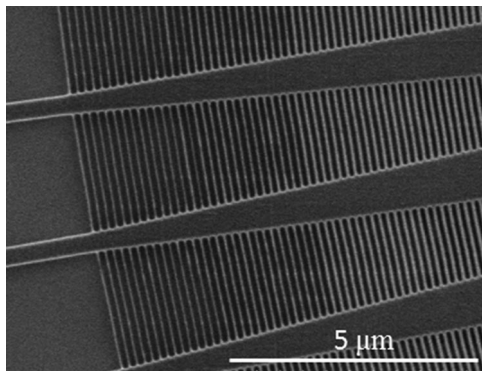


Figure 18 SEM image of a SWG mode converter for coupling between the free space propagation region and the array waveguides of an arrayed waveguide grating. The gradual transition facilitates efficient coupling between both regions.

study of these mode converters confirmed the measured performance [47, 157]. Using rigorous coupled wave analysis and bi-directional mode expansion propagation the authors calculated a theoretical reflectivity of only -43.8 dB and a transmission of over 99% (0.04 dB loss).

SWG mode converters have also been used as gradual transitions between continuous fields and discretized fields [158]. For example, the main source of internal loss in an arrayed waveguide grating is the coupling between the slab waveguide and the array waveguides. As the continuous field in the slab waveguide combiner of an arrayed waveguide grating propagates across the slab–array boundary, it couples to the discretized field of the array waveguides. The corresponding loss is particularly significant in high-index-contrast waveguides where the strong confinement results in an increased mode mismatch. A judiciously designed SWG can facilitate efficient mode coupling between a slab waveguide and a waveguide array. Figure 18 shows a SEM image of the SWG transition region with a theoretical loss penalty of 0.2 dB [158].

4.3. Fourier transform spectrometer chip

The combination of SWG waveguides and conventional waveguides provides an additional degree of freedom in device design. As an example, a planar Fourier transform spectrometer based on an array of Mach–Zehnder interferometers (MZIs) is considered here. This device operates as follows. MZIs across the array exhibit an increased imbalance by a constant length increment. Light intensity measured across different outputs of MZIs constitutes the spatial interferogram and the input light spectrum is calculated as the inverse Fourier transform of the interferogram [159]. Instead of using bends to produce an optical path imbalance by a length difference, a SWG waveguide can be used in one arm to produce an optical path imbalance by an effective mode index difference [160]. This approach allows for a compact layout of densely arrayed MZIs (all parallel waveguides, no bends) in a small device footprint.

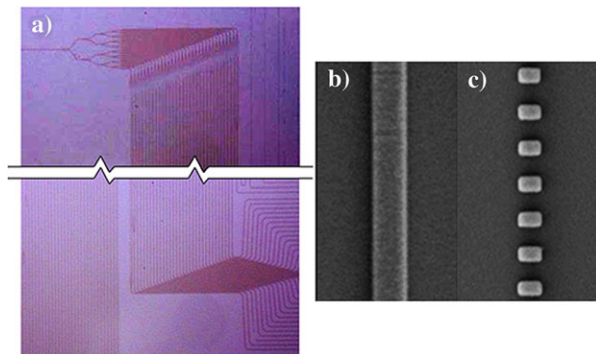


Figure 19 Optical and SEM images of a Fourier transform interferometer array. (a) The fabricated array of 32 MZIs showing the cascaded Y-splitters and the output waveguide fan-out (break lines are included as the actual device is very long). (b) Strip waveguide detail of one arm (width 450 nm) and (c) the SWG detail (width 300 nm, pitch 400 nm, duty cycle 50%) of the other arm of a MZI.

The fabricated device, shown in Fig. 19, comprises an array of 32 MZIs, which produce a spatial interferogram without any moving parts, yielding a spectral resolution of 50 pm and a free-spectral range of 0.78 nm. As a result of similar propagation losses in SWG waveguides and in conventional strip waveguides, loss imbalance is minimized and high interferometric extinction ratios of 25 to 30 dB are obtained. Furthermore, phase and amplitude errors arising from typical fabrication errors are compensated by the spectral retrieval process using calibration measurements [160, 161].

4.4. Ultra-fast optical switching

MZIs with a lower arm comprising a SWG waveguide and an upper arm a conventional strip waveguide have also been used to demonstrate ultra-fast optical switching [162]. In the SWG arm of the MZI, the waveguide mode is delocalized resulting in a lower optical density in the silicon core compared to the MZI arm with the conventional strip waveguide. This optical density difference results in differential nonlinear self-phase modulation between the two arms of the interferometer, and the relative phase shift π required for an on/off switch can be obtained. Optical and SEM images of the fabricated device are shown in Fig. 20. Back-to-back SWG mode converters were also included in the conventional strip waveguide arm to mitigate loss imbalance and spectral dependence that may arise if the SWG mode converters were only included in the MZI arm with SWG waveguides. The device was experimentally characterized by combining a high-power pump with a low-power probe signal. The combined input was split 50 : 50 by a Y-branch into both arms. A Peltier cooler was used to tune the MZI to a dark fringe (the off condition), i.e. a π phase shift between the two arms. When the high-power pump was on, the strip waveguide arm experienced self-phase modulation resulting in an additional phase increment π (the on

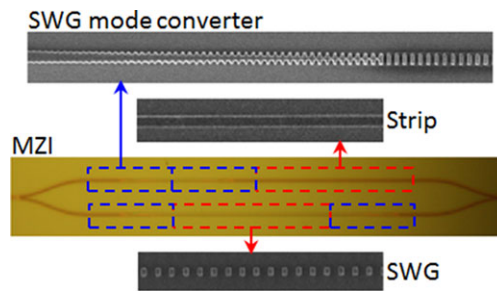


Figure 20 Optical image of a fabricated 1 THz optical switch based on self-phase modulation. The upper arm comprises a strip waveguide and back-to-back SWG mode converters. The lower arm consists of a SWG waveguide with SWG mode converters in both ends.

condition). All-optical switching at ~ 1 Tb/s data rates for a pump power of 3.3 W was successfully demonstrated.

4.5. Waveguide modulators

SWG structures have also been exploited for making active silicon-based devices. Notable examples are high-speed silicon modulators, based on partially doped waveguides into which carriers are injected to produce a change in refractive index. In these waveguides a trade-off between modal confinement and a low electrical resistance between the waveguide and the electrodes needs to be found. This is usually achieved by using rib waveguides, with the slab acting as electrical contact between the electrodes and the waveguide core. Such structures are, however, quite sensitive to etch depth variations. Recently, the use of fully etched, sub-wavelength sidewall gratings was proposed to substitute the partially etched slab, thereby easing the fabrication process of the modulator structure [163].

4.6. MMI couplers

MMI couplers are fundamental building blocks in many photonic circuits, including resonators, coherent transmitters and receivers, sensors, etc. [164–166]. This section focuses on the optimization of MMI couplers by means of lengthwise SWGs. As opposed to the previous sections where mostly single-mode devices were considered, for MMI couplers it is essential to consider multimode propagation in SWGs. The fundamentals of MMI couplers are briefly reviewed in Section 4.6.1. High-performance MMI couplers for coherent communications are discussed in Section 4.6.2 and ultra-compact MMI devices are described in Section 4.6.3.

4.6.1. MMI fundamentals

Consider the MMI coupler shown schematically in Fig. 21. When light is injected in any of the input ports (ϕ_{in}) it excites

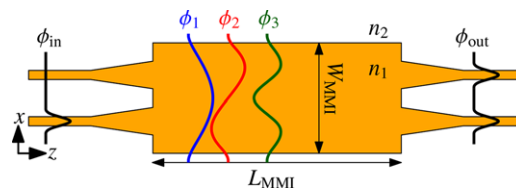


Figure 21 Schematic of a 2×2 MMI coupler. The input field, ϕ_{in} , excites multiple modes in the central region, ϕ_1, ϕ_2, \dots , which after propagating a distance L_{MMI} form a double image of the input field that is coupled to the modes of the output waveguides, ϕ_{out} .

a linear combination of the guided modes of the central region (ϕ_1, ϕ_2, \dots). These modes propagate through the structure with different propagation constants (β_m), forming single or multiple replicas (images) of the input excitation field, in a process known as self-imaging or the Talbot effect [167]. By placing the output waveguides at the positions of the images, power splitting is achieved. The length of the device (L_{MMI}) is therefore determined by the position of the output plane where the images are formed, which in turn is proportional to the beat length (L_π) of the lowest order modes of the multimode region at a specific wavelength:

$$L_\pi(\lambda) = \frac{\pi}{\beta_1(\lambda) - \beta_2(\lambda)}. \quad (8)$$

For high-quality imaging it is furthermore required that the propagation constants of the modes satisfy the quadratic relation

$$\beta_m = \beta_1 - (m^2 - 1)\pi/(3L_\pi). \quad (9)$$

Usually only the lower order modes fulfill this condition [168], so that the use of tapered input waveguides (see Fig. 21) that only excite a limited number of (lower order) modes is common practice in MMI coupler design.

4.6.2. High-performance MMI with SWG lateral cladding

The core-cladding refractive index contrast of the multimode waveguide, $\Delta n = n_1 - n_2$, strongly affects the number of modes that fulfill Eq. (9), and consequently it is a fundamental parameter in determining MMI performance [168]. When Δn is very large, as is the case in the silicon-on-insulator platform, the higher order modes do not properly contribute to image formation, degrading device response. This drawback is especially relevant for MMI couplers with more than two input and output ports, where the fraction of power carried by the higher order modes becomes significant.

The lateral refractive index contrast of the MMI coupler can be reduced using a shallow etch to define the multimode region [165]. Although this technique clearly improves the device performance, it adds complexity in the fabrication process, since it requires multiple etch steps. Furthermore,

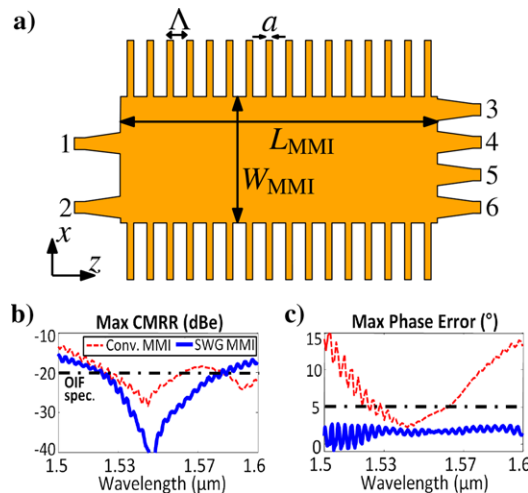


Figure 22 A 2×4 MMI coupler with a lateral SWG cladding that minimizes modal phase errors and improves device performance. (a) Geometry of the device as proposed in [169]. (b) Simulated maximum common mode rejection ratio and (c) simulated maximum phase error between the output ports.

the shallow etch depth needs to be accurately controlled in order to obtain the target value of the index contrast.

A different approach to reduce the lateral index contrast is to use a lengthwise SWG in the lateral cladding regions of the MMI coupler, as shown in Fig. 22a [169]. By properly designing the pitch and duty cycle of the SWG, the optimal lateral cladding effective index can be synthesized. Compared with the shallow etch MMI coupler proposed in [165], this approach has two important advantages: (i) the MMI coupler can be fabricated using the same single full etch depth as other components on the chip (e.g. interconnection waveguides) and (ii) the SOI BOX acts as a natural etch stop layer, so the etch depth is accurately controlled.

Using the SWG approach, a 2×4 MMI coupler that works as a 90° hybrid for coherent optical reception was designed [169]. The dimensions of the device are $W_{\text{MMI}} = 7.7 \mu\text{m}$, $\Delta = 240 \text{ nm}$, $a = 180 \text{ nm}$, and $L_{\text{MMI}} = 117.6 \mu\text{m}$. Simulation results confirmed the superior performance of the SWG-engineered MMI coupler. The performance of a 90° hybrid is often quantified in terms of the common mode rejection ratio (CMRR) and phase error. Denoting by p_i the power at each output (see Fig. 22), the CMRR for the in-phase channel is defined as $\text{CMRR (dBe)} = 20 \log_{10}[(p_3 - p_6)/(p_3 + p_6)]$, when power is launched from either input (the CMRR is measured in electrical decibels (dBe), hence the factor of 20). For the quadrature channel p_3 and p_6 are substituted by p_4 and p_5 , respectively. The overall CMRR is then given by maximum (worst) CMRR of the in-phase and quadrature channels. Defining φ_i as the relative phase with which waves from inputs 1 and 2 combine at outputs $i = 3, \dots, 6$, the relevant phase errors of the hybrid are $\varphi_6 - \varphi_3 - 180^\circ$, $\varphi_5 - \varphi_4 - 180^\circ$, and $\varphi_6 - \varphi_5 - 90^\circ$. Figures 22b and c compare the wavelength responses of the MMI coupler with SWG cladding and a conventional MMI coupler of the same width. The

device covers the C-band (1530–1570 nm) with a maximum CMRR lower than -24 dBe and a maximum phase error between output ports of less than 2° . This performance exceeds the Optical Internetworking Forum specifications [170], which require CMRR and phase error of less than -20 dBe and $\pm 5^\circ$, respectively. In contrast, the conventional MMI coupler design, with a bandwidth of 36 nm, failed to cover the C-band. An implementation of a 2×4 MMI coupler with SWG cladding exhibiting an enhanced operational bandwidth of 60 nm was recently reported [171].

4.6.3. Compact 2×2 MMI coupler with SWG slot

Sub-wavelength engineering can furthermore be used to reduce the size of MMI couplers by a factor of two, without affecting device performance. The principle is as follows. In a MMI coupler that is excited off-center, the first replica of the input field (bar state) appears at a distance $z = L_{\text{bar}} = 6L_\pi$. At this point, the phase difference between the even modes ($\phi_1, \phi_3, \phi_5, \dots$) and the odd modes ($\phi_2, \phi_4, \phi_6, \dots$) is a multiple of 2π [167]. The first single inverted self-image (cross state) occurs at a distance $z = L_{\text{cross}} = L_{\text{bar}}/2$, and the phase difference is an odd multiple of π . The MMI coupler works as a 3 dB coupler at half of this distance $z = L_{3\text{dB}} = L_{\text{cross}}/2 = L_{\text{bar}}/4$. The length of a MMI coupler can be reduced if a small perturbation is introduced to modify these modal phase relations without significantly affecting the mode profiles. For example, it has been proposed that, using a narrow lengthwise slot at the center of the multimode region, device length is shortened by a factor of two [172, 173]. The slot modifies the propagation constants of the even modes since they have maximum intensity distribution along the slot, but does not affect the odd modes, as their intensity is zero at the center of the multimode region. By adjusting the slot refractive index, the phase relations between even and odd modes can be set to obtain a bar state at half the distance compared to conventional MMI devices. By doing so, the length of a slotted MMI 3 dB coupler can also be halved. The main challenge of this elegant approach is the practical implementation of the slot, which involves the use of an additional shallow etch depth that complicates the fabrication process [172].

To circumvent this problem an implementation with a SWG slot has been proposed [174]. The idea is to synthesize the slot using a lengthwise SWG row of holes, as schematically shown in Fig. 23a. The holes are fully etched down to bottom oxide in a single etch step process. Since the structure is sub-wavelength, it acts as a homogeneous lengthwise slot with an equivalent refractive index which depends on the grating pitch and duty cycle.

This approach was experimentally validated with a SWG-slotted MMI 3 dB coupler [174]. The dimensions of the SWG structure were initially calculated using Rylov's formulas and then optimized using a numerical tool [46]. Structural parameters of the fabricated device are: MMI width $W_{\text{MMI}} = 3.5 \mu\text{m}$, width of the access ports $W_A = 1.5 \mu\text{m}$, pitch $\Delta = 238 \text{ nm}$, and square holes of

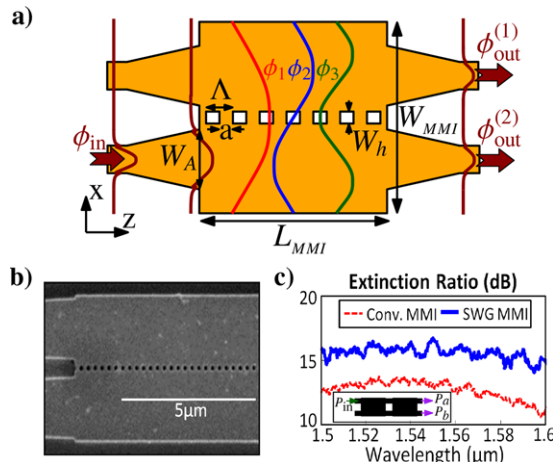


Figure 23 Ultra-compact 2×2 MMI coupler based on a central sub-wavelength slot that reduces the length of the device by a factor of two without affecting performance. (a) Geometry of the device as proposed in [174]. (b) Experimental implementation – SEM image of a fabricated device. (c) Measured extinction ratio of the device in back-to-back configuration. Extinction ratio is defined as $10 \log_{10} P_b/P_a$, with P_a and P_b defined in the inset.

size $50 \times 50 \text{ nm}^2$. The length of the shortened device is $L_{\text{MMI}} = 22.85 \mu\text{m}$, which is close to half of the length of the conventional MMI coupler of the same width used as reference ($L_{\text{MMI}}^{\text{conv}} = 47 \mu\text{m}$). Figure 23b shows a SEM image of a fabricated device. A back-to-back configuration was used to measure the extinction ratio, from which the power imbalance and the phase error were estimated. As shown in Fig. 23c the SWG-slotted MMI coupler exhibits a slightly superior extinction ratio to the conventional device, so the size reduction does not result in any penalty in device performance. Within the C-band, estimated power imbalance and phase error for the shortened MMI coupler are $\sim 1.3 \text{ dB}$ and $\sim 5^\circ$, respectively, marginally better than those of the conventional MMI coupler ($\sim 1.7 \text{ dB}$ and $\sim 6^\circ$).

4.7. Dispersion engineered ultra-broadband couplers

Within the SWG regime, two zones with qualitatively different dispersion behavior can be identified, as shown in Fig. 24. For wavelengths $\lambda \gg \Lambda$ (deep sub-wavelength), n_B is nearly constant, so the dispersion of the equivalent homogeneous material is low and mainly determined by the material dispersion. This is the zone that has been exploited in the applications discussed up to this point in this article. However, when λ approaches the Bragg condition the slope of the $n_B(\lambda)$ curve increases rapidly, and the sub-wavelength structure behaves as a material with a large and adjustable chromatic dispersion. It is in this region where SWG structures can be used to design ultra-broadband directional couplers (DCs) and MMI devices.

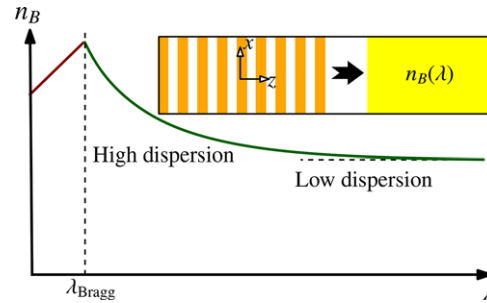


Figure 24 Dispersion curve of a multilayer medium operating from the sub-wavelength regime (right-hand side) to Bragg regime (left-hand side). The inset illustrates the homogenization process, which leads to an artificial material with chromatic dispersion and equivalent refractive index $n_B(\lambda)$.

Both DCs and MMI couplers are fundamental functional blocks in integrated photonics. Although the physical principles governing DCs and MMI couplers are quite different, both devices share a common characteristic: their physical lengths are designed to be proportional to the beat length of the two lowest order modes at a specific wavelength, i.e. $L_{\text{device}} \propto L_\pi(\lambda_0)$, where $L_\pi(\lambda_0) = \pi/[\beta_1(\lambda_0) - \beta_2(\lambda_0)]$ (see Section 4.6.1). Since the wavelength dependence of the propagation constants depends on the mode number (i.e. $d\beta_1/d\lambda \neq d\beta_2/d\lambda$), $L_\pi(\lambda)$ is wavelength dependent. The bandwidth of these structures is therefore limited by the wavelength sensitivity of the beat length. Several techniques to enhance the operational bandwidth of DCs can be found in the literature [175–178]. In contrast, optimization of the MMI coupler bandwidth has received comparatively little attention, probably because these devices intrinsically exhibit a much broader bandwidth than DCs. In the following it will be shown how the characteristic dispersive properties of SWG structures can be used to significantly increase the bandwidth of DCs and MMI devices.

4.7.1. Colorless directional coupler

Figure 25 shows the geometry of the broadband (colorless) DC proposed in [179]. It is composed of two coupled waveguides embedded in a lengthwise SWG structure. The key point in this implementation is that the SWG exerts different effects on the propagation constants β_1 and β_2 of the even and the odd supermodes ϕ_1 and ϕ_2 . The field profile of the odd supermode (ϕ_2) is asymmetric, so the effect on β_2 of the SWG region between the waveguides is minimal. Conversely, the even supermode (ϕ_1) propagation constant β_1 is significantly affected by the dispersion behavior of the SWG, so the even mode dispersion can be tailored to achieve nearly the same wavelength dependence as the odd mode (i.e. $d\beta_1/d\lambda \approx d\beta_2/d\lambda$). In this way, the wavelength dependence of the beat length $L_\pi(\lambda)$ is reduced, thus increasing the operational bandwidth of the

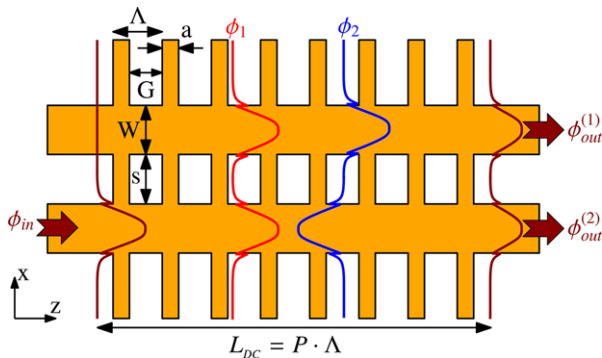


Figure 25 Geometry of the colorless DC as proposed in [179]. The dispersion of the sub-wavelength structure compensates the dispersion of the coupled waveguides, resulting in broadband behavior.

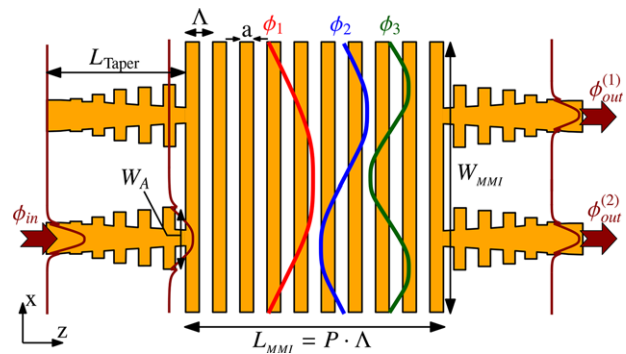


Figure 27 Geometry of the ultra-broadband MMI coupler as proposed in [20]. The segmented central region is optimized to provide a wavelength-independent beat length, thereby enhancing the operational bandwidth. The tapered SWG input and output waveguides provide effective index matching between the conventional Si-wire waveguides and the segmented central region.

device. This concept was applied in [179] to design a colorless SWG DC. Dimensional parameters of the optimized device are $W = 450$ nm, $s = 500$ nm, $\Lambda = 270$ nm, duty cycle $a/\Lambda = 22.5\%$, and length $L_{DC} = 71\Lambda = 19.2$ μm . The minimum feature size is greater than 60 nm and the device can be fabricated using electron-beam lithography. In Fig. 26 the wavelength dependence of this device is compared with that of a conventional DC of similar length. The nearly flat L_π curve of the SWG DC shown in Fig. 26a predicts a broadband response, which is confirmed in Fig. 26b. The SWG DC covers a 100 nm bandwidth with a power imbalance less than 0.6 dB. On the contrary, the strong variation of L_π in the conventional DC severely limits its bandwidth, which is smaller than 20 nm.

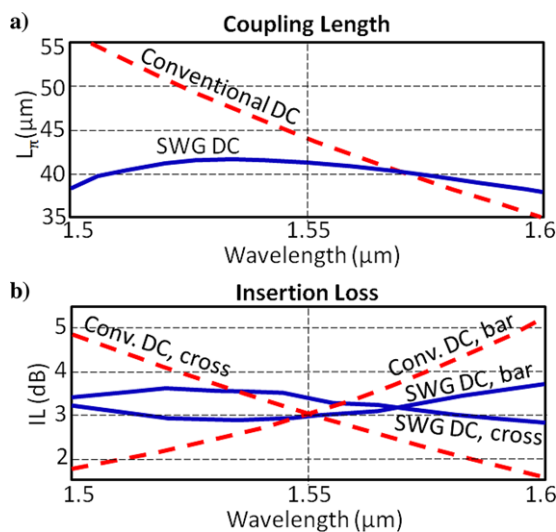


Figure 26 (a) Comparison of the beat lengths of a conventional DC and the SWG-assisted coupler, showing reduced wavelength dependence. (b) Simulated insertion losses (3 dB ideal) of a conventional DC and the SWG-assisted device.

4.7.2. Ultra-broadband MMI couplers

Although MMI couplers require multiple guided modes to achieve image formation (as opposed to the two supermodes in a DC) the condition of achieving $L_\pi \sim \text{constant}$ with wavelength suffices to warrant broadband operation. This can be achieved with the MMI geometry shown in Fig. 27 [20]. In this device, the central multimode region is a lengthwise SWG waveguide of width $W_{MMI} = 6$ μm , pitch $\Lambda = 198$ nm, and duty cycle of 50%. The tapered SWG transitions at both sides of the multimode region are particularly important, since they provide an adiabatic transition between the interconnecting waveguides (conventional Si wires of width 450 nm) and the SWG access ports of width $W_A = 1.2$ μm . These tapers are similar to those proposed in [15, 156, 157] and exhibit negligible losses for a taper length $L_{taper} = 10$ μm .

Figure 28a compares the beat lengths (L_π) of the SWG-engineered MMI coupler and a conventional MMI coupler of the same width. The SWG device shows a nearly flat beat length $L_\pi(\lambda) \sim 40$ μm for wavelengths from 1.26 to 1.7 μm , whereas for the conventional MMI L_π varies between 120 and 80 μm . The impact of the virtually flat $L_\pi(\lambda)$ on the operating bandwidth of the optimized device is evident from the simulation results shown in Fig. 28b. The SWG MMI coupler exhibits an ultra-broad bandwidth of 450 nm, covering all optical bands (O, E, S, C, L, and U) with insertion loss, power imbalance, and phase error below 1 dB, 0.6 dB, and 3°, respectively.

Finally, it is worth noting an additional advantage of the SWG MMI coupler: it is significantly shorter than the conventional device ($L_{MMI}^{\text{SWG}} = 18.6$ μm versus $L_{MMI}^{\text{conv}} = 48.2$ μm). The shortening of the SWG-based device is a consequence of the lower equivalent refractive index of the SWG multimode region when compared with the homogeneous silicon core of the conventional MMI coupler [20].

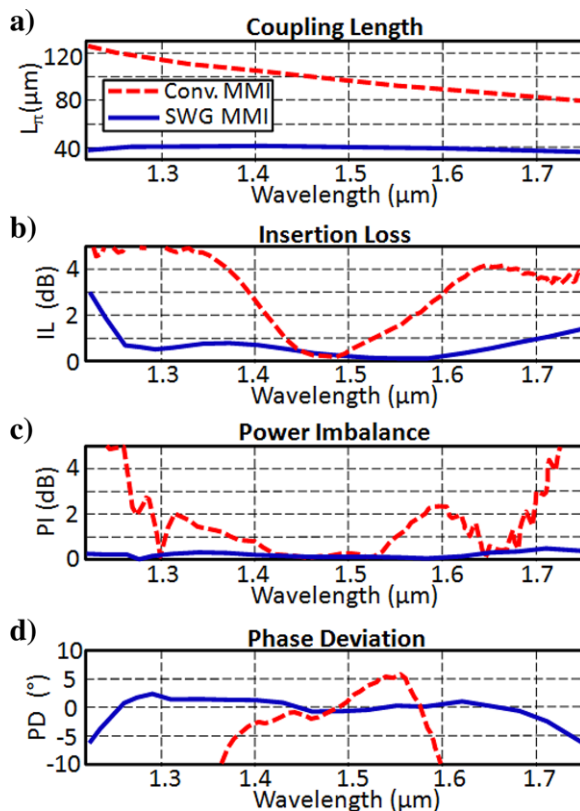


Figure 28 Simulated performance of the ultra-broadband MMI coupler compared to a conventional device. (a) Beat length, (b) insertion loss, (c) power imbalance, and (d) phase deviation.

5. Conclusions

Sub-wavelength structures are becoming of fundamental importance in integrated photonics. Their ability to control material refractive index and birefringence simply by lithographic patterning has enabled new design strategies that have led to advanced devices with some of the best ever reported combinations of compactness and performance, for different applications, including fiber-chip coupling, waveguide crossings, polarization control, on-chip spectrometers, and MMI couplers, to name a few. It is also apparent that dispersion engineering with SWGs has an excellent potential to dramatically increase the operational bandwidth of a variety of photonic devices. Fabrication of SWG structures is not limited to expensive high-resolution techniques such as electron-beam lithography, but is amendable to mass production as several SWG-based devices have already been successfully fabricated with DUV stepper lithography. The continuing improvement in advanced lithography techniques (such as immersion lithography or extreme-UV lithography) will enable accurate, large-volume production of SWG structures and devices. The use of SWG structures in integrated photonics devices is thus likely to continue to expand, enabling new functionalities and devices to be designed and fabricated, and these SWG structures will become an essential tool set in advanced photonic design libraries.

Acknowledgement. This work was supported by the Spanish Ministry of Science under project TEC2013-46917-C2-1-R, the Andalusian Regional Ministry of Science, Innovation and Business under project P09-TIC-5268, and the National Research Council of Canada. The authors would like to acknowledge the contributions of Alejandro Maese-Nov, Luis Zavargo-Peche, Diego Pérez-Galacho, and Sebastian Romero-García to the design of several of the devices presented here. We furthermore thank Diego Pérez-Galacho for insightful discussions on silicon modulators.

Received: 1 April 2014, **Revised:** 17 July 2014,

Accepted: 7 August 2014

Published online: 1 October 2014

Key words: Sub-wavelength structures, index engineering, dispersion engineering, grating couplers, wavelength demultiplexers, anti-reflective coatings, broadband waveguide couplers, waveguide crossings, athermal waveguides.



Robert Halir received an MSc in telecommunications engineering with first-class honors from Málaga University (Spain) in 2006. In the same year, he was awarded a FPU scholarship to carry out his thesis in silicon photonics. His work focused on the design and characterization of an integrated optical reflectometer, for which he received a PhD from the same university in 2010. Currently he is an assistant professor at Málaga University, as well as a researcher at the Andalusian Institute for Nano-medicine and Biotechnology (Bionand). His research currently focuses on high-performance silicon photonic devices, including ultra-broadband couplers, highly efficient fiber-chip couplers, and photonic biosensors.



Przemek J. Bock is currently a photonics engineer at CMC Microsystem, a technology broker helping academic and industry clients develop microsystems primarily in the area of integrated electronics and photonics. After working for Optiwave as a software developer designing photonics modeling applications, he received a PhD from the University of Ottawa where he worked at the National Research Council of Canada developing sub-wavelength gratings as well as spectrometers for the silicon-on-insulator material platform. In his postdoctoral period he worked in industry developing silicon photonics devices for the aerospace industry.



Pavel Cheben is a senior research officer at the National Research Council of Canada. He is also an adjunct professor at Carleton University, McMaster University, Complutense University of Madrid, and University of Malaga. His present research interest includes silicon photonics, planar waveguide circuits, and sub-wavelength structures. He was one of the

scientists that helped start Optenia Inc. and developed the first commercial echelle grating wavelength division multiplexer. He has co-authored 13 book chapters, more than 250 papers in journals and conference proceedings, and over 20 patent applications, and served as an editor of several journal special issues and conference proceedings.



Alejandro Ortega-Moñux received an MSc in telecommunications engineering from Málaga University (Spain) in 1998 and a PhD from the same university in 2008. Since 1999 he has been with ETSI Telecomunicación, Universidad de Málaga, as an assistant and then associate professor. His research interest is in the area of the modeling and design of photonic integrated circuits, such as multimode interference couplers, fiber-chip grating couplers, polarization beam splitters and rotators or sub-wavelength periodic structures.



Carlos Alonso-Ramos received an MSc in telecommunications engineering from Málaga University (Spain) in 2008. Since 2009 he has been carrying out work for a PhD on integrated photonic circuits. Currently he is working under a FPI scholarship supervised by Dr. Alejandro Ortega. His main task is coupling diffraction gratings design. In collaboration with the National Research Council of Canada (NRC), he has demonstrated efficient grating couplers in thick rib silicon-on-insulator waveguides for the first time. He also works on integrated polarization diversity management circuits. Together with the Heinrich Hertz Institute in Germany, he has developed a waveguide polarization rotator with simplified fabrication process. Together with the NRC and the Institut d'Electronique Fondamentale in the University of Paris Sud in France, he has developed a new polarization rotation scheme with increased fabrication tolerances.



Jens H. Schmid is a research officer with the Information and Communications Technologies portfolio of the National Research Council of Canada (NRC) and also an adjunct professor with the Department of Electronics at Carleton University. He received a PhD from the University of British Columbia in 2004 for his work on in-situ etching and molecular beam epitaxial regrowth on III-V semiconductors.

After working for a year as a research scientist for VSM MedTech, a medical device company in Coquitlam, British Columbia, where he developed fabrication processes for superconducting quantum interference devices, he joined the nanofabrication group at NRC in 2005. His current research interests are the fabrication, design, characterization, and simulation of silicon photonic devices and nanostructures.



Jean Lapointe received a PhD in physics from SUNY at Stony Brook (1993) studying quantum effects in macroscopic systems at low temperatures (SQUIDs). He then joined the National Research Council of Canada in Ottawa working on the fabrication and measurement of single electron circuits for applications in metrology. He then joined the nanofabrication effort and is now senior research officer and leader of a micro/nano fabrication team within the Information and Communications portfolio. His research focuses on the use of electron-beam lithography and the fabrication of micro- and nano-devices for applications in the areas of silicon photonics, nano-photonics, nano-electronics, semiconductor lasers, and GaN-based electronics.



Dan-Xia Xu is a principal research officer with the National Research Council of Canada (NRC), and an adjunct professor with Carleton University. She received a PhD from Linköping University (Sweden) in 1991 working on silicon-germanium heterojunction bipolar transistors (HBTs) and tunneling diodes. Since joining NRC, she has developed high-speed SiGe HBTs and SiGe and silicide photodetectors, and pioneered the use of nickel silicide for deep sub-micrometer very-large-scale integration. She later switched her research to integrated optics. In 2001–2002 she was part of the research team at Optenia Inc. that successfully developed the first commercial glass waveguide echelle grating demultiplexer. Since 2003, she has led pioneering work in using cladding stress-induced birefringence for polarization control in silicon-on-insulator waveguide components, and in evanescent field waveguide biosensors on the silicon-on-insulator platform. Her current research interest is silicon photonics and photonic integration for optical communications and biological sensing. She has co-authored over 300 publications and several book chapters, and holds seven patents.



J. Gonzalo Wangüemert-Pérez received a telecommunication engineer degree (MSc in telecommunication engineering) from the Universidad Politécnica de Madrid (Spain) in 1992, and a PhD from the Universidad de Málaga (Spain) in 1999. Since 1993, he has been with ETSI Telecomunicación (Universidad de Málaga), first an assistant professor and then as associate professor. His research activity mainly involves the area of modeling and design of photonic integrated circuits, including also the development of electromagnetic tools for analysis, modeling, and simulation of integrated photonic devices.



Íñigo Molina-Fernández is full professor and leader of the photonics group at the University of Málaga, Spain. He is co-author of more than 70 international publications in microwave and photonic topics. He has participated in more than 25 research and development national and international projects, being the leader of 12 of them.



Siegfried Janz received a PhD in physics (in surface nonlinear optics) in 1991 from the University of Toronto, Canada. He then joined the National Research Council of Canada (NRC), Ottawa, where he worked on nonlinear frequency conversion and optical switching in III-V semiconductor waveguides, and silicon-based optoelectronics. During 2001–2002, he was part of the research team with Optenia Inc. that successfully developed the first glass waveguide echelle grating demultiplexer. He is presently the program leader of the Advanced Photonic Component Program at NRC, and also an adjunct professor with the Department of Electronics of Carleton University. His current research interests include active and passive integrated optics, and in particular silicon photonic devices for applications in optical communications and biological sensing.

References

- [1] H. Hertz, *Wiedemanns Ann.* **36**, 769 (1888).
- [2] L. Rayleigh, *Phil. Mag.* **34**, 481–502 (1892).
- [3] I. E. Tamm and V. L. Ginzburg, *Izv. Akad. Nauk SSSR* **7**, 30–51 (1943).
- [4] S. M. Rytov, *Sov. Phys. JETP* **2**, 466–475 (1956).
- [5] C. Bernhard and W. H. Miller, *Acta Physiol. Scand.* **56**, 385–386 (1962).
- [6] P. Clapham and M. Hutley, *Nature* **244**, 281–282 (1973).
- [7] J. N. Mait and D. W. Prather, *Selected Papers on Subwavelength Diffractive Optics* (SPIE Optical Engineering Press, Bellingham, WA, 2001).
- [8] P. Yeh, *Opt. Commun.* **26**, 289–292 (1978).
- [9] E. B. Grann, M. G. Moharam, and D. A. Pommet, *J. Opt. Soc. Am. A* **11**, 2695–2703 (1994).
- [10] S. Wilson and M. Hutley, *J. Mod. Opt.* **29**, 993–1009 (1982).
- [11] R. C. Enger and S. K. Case, *Appl. Opt.* **22**, 3220–3228 (1983).
- [12] M. E. Motamedi, W. H. Southwell, and W. J. Gunning, *Appl. Opt.* **31**, 4371–4376 (1992).
- [13] J. Van der Ziel, *Appl. Phys. Lett.* **26**, 60–62 (1975).
- [14] A. Fiore, V. Berger, E. Rosencher, P. Bravetti, and J. Nagle, *Nature* **391**, 463–466 (1998).
- [15] P. Cheben, P. J. Bock, J. H. Schmid, J. Lapointe, S. Janz, D. Z. Xu, A. Densmore, A. Delâge, B. Lamontagne, and T. J. Hall, *Opt. Lett.* **35**, 2526–2528 (2010).
- [16] R. Halir, P. Cheben, S. Janz, D. X. Xu, Í. Molina-Fernández, and J. G. Wangüemert-Pérez, *Opt. Lett.* **34**, 1408–1410 (2009).
- [17] M. C. Huang, Y. Zhou, and C. J. Chang-Hasnain, *Nat. Photonics* **1**, 119–122 (2007).
- [18] P. J. Bock, P. Cheben, J. H. Schmid, J. Lapointe, A. Delâge, D. X. Xu, S. Janz, A. Densmore, and T. J. Hall, *Opt. Express* **18**, 16146–16155 (2010).
- [19] J. Wang, I. Glesk, and L. R. Chen, *Opt. Express* **22**, 15335–15345 (2014).
- [20] A. Maese-Novo, R. Halir, S. Romero-García, D. Pérez-Galacho, L. Zavargo-Peché, A. Ortega-Moñux, I. Molina-Fernández, J. Wangüemert-Pérez, and P. Cheben, *Opt. Express* **21**, 7033–7040 (2013).
- [21] E. G. Loewen and E. Popov, *Diffraction Gratings and Applications* (CRC Press, Boca Raton, FL, 1997).
- [22] P. Cheben, in: *Optical Waveguides: From Theory to Applied Technologies*, edited by M. L. Calvo and V. Lakshminarayanan (CRC Press, Boca Raton, FL, 2006), chap. 5, pp. 173–230.
- [23] T. Tamir and S. Peng, *Appl. Phys.* **14**, 235–254 (1977).
- [24] D. Rosenblatt, A. Sharon, and A. A. Friesem, *IEEE J. Quantum Electron.* **33**, 2038–2059 (1997).
- [25] A. E. Miroshnichenko, S. Flach, and Y. S. Kivshar, *Rev. Mod. Phys.* **82**, 2257–2298 (2010).
- [26] R. Kashyap, *Fiber Bragg Gratings* (Academic Press, San Diego, CA, 1999).
- [27] J. D. Joannopoulos, S. G. Johnson, J. N. Winn, and R. D. Meade, *Photonic Crystals: Molding the Flow of Light* (Princeton University Press, Princeton, NJ, 2011).
- [28] D. H. Raguin and G. M. Morris, *Appl. Opt.* **32**, 1154–1167 (1993).
- [29] P. Lalanne, S. Astilean, P. Chavel, E. Cambril, and H. Launois, *J. Opt. Soc. Am. A* **16**, 1143–1156 (1999).
- [30] P. Lalanne and D. Lemercier-Lalanne, *J. Mod. Opt.* **43**, 2063–2085 (1996).
- [31] P. Lalanne and J. P. Hugonin, *J. Opt. Soc. Am. A* **15**, 1843–1851 (1998).
- [32] X. Letartre, J. Mouette, J. Leclercq, P. R. Romeo, C. Seassal, and P. Viktorovitch, *J. Lightwave Technol.* **21**, 1691–1699 (2003).
- [33] A. Hessel and A. A. Oliner, *Appl. Opt.* **4**, 1275–1297 (1965).
- [34] G. Golubenko, A. Svakhin, V. Sychugov, and A. Tishchenko, *Sov. J. Quantum Electron.* **15**, 886–887 (1985).
- [35] S. Goeman, S. Boons, B. Dhoedt, K. Vandepitte, K. Caekebeke, P. Van Daele, and R. Baets, *IEEE Photonics Technol. Lett.* **10**, 1205–1207 (1998).
- [36] R. Baets, B. Demeulenaere, B. Dhoedt, and S. Goeman (US patent 6191890B1, 2001).
- [37] H. Hattori, X. Letartre, C. Seassal, P. Rojo-Romeo, J. Leclercq, and P. Viktorovitch, *Opt. Express* **11**, 1799–1808 (2003).
- [38] C. F. Mateus, M. C. Huang, Y. Deng, A. R. Neureuther, and C. J. Chang-Hasnain, *IEEE Photonics Technol. Lett.* **16**, 518–520 (2004).
- [39] S. Fan, J. D. Joannopoulos, J. N. Winn, A. Devenyi, J. C. Chen, and R. D. Meade, *J. Opt. Soc. Am. B* **12**, 1267–1272 (1995).
- [40] S. F. Helpert and R. Pregla, *J. Lightwave Technol.* **16**, 1694–1702 (1998).
- [41] S. G. Johnson and J. D. Joannopoulos, *Opt. Express* **8**, 173–190 (2001).

- [42] J. Čtyroký, S. Helfert, R. Pregla, P. Bienstman, R. Baets, R. De Ridder, R. Stoffer, G. Klaasse, J. Petráček, P. Lalanne, J. Hugonin, and R. De LaRue, *Opt. Quantum Electron.* **34**, 455–470 (2002).
- [43] J. Hugonin, P. Lalanne, I. D. Villar, and I. Matias, *Opt. Quantum Electron.* **37**, 107–119 (2005).
- [44] G. Lecamp, J. P. Hugonin, and P. Lalanne, *Opt. Express* **15**, 11042–11060 (2007).
- [45] K. Yasumoto, *Electromagnetic Theory and Applications for Photonic Crystals* (CRC Press, Boca Raton, FL, 2010).
- [46] L. Zavargo-Peche, A. Ortega-Moñux, J. Wangüemert-Pérez, and I. Molina-Fernández, *Prog. Electromagn. Res.* **123**, 447–465 (2012).
- [47] J. Ctyroky, *J. Lightwave Technol.* **30**, 3699–3708 (2012).
- [48] J. D. Joannopoulos, S. G. Johnson, J. N. Winn, and R. D. Meade, *Photonic Crystals: Molding the Flow of Light* (Princeton University Press, Princeton, NJ, 2011).
- [49] P. Yeh, A. Yariv, and C. S. Hong, *J. Opt. Soc. Am. A* **67**, 423–438 (1977).
- [50] S. Wang, *IEEE J. Quantum Electron.* **10**, 413–427 (1974).
- [51] J. L. Jewell, J. Harbison, A. Scherer, Y. Lee, and L. Florez, *IEEE J. Quantum Electron.* **27**, 1332–1346 (1991).
- [52] D. Taillaert, P. Bienstman, and R. Baets, *Opt. Lett.* **29**, 2749–2751 (2004).
- [53] L. Li and J. J. Burke, *Opt. Lett.* **17**, 1195–1197 (1992).
- [54] Z. Weissman and I. Hendel, *J. Lightwave Technol.* **13**, 2053–2058 (1995).
- [55] B. J. Offrein, G. L. Bona, R. Germann, I. Massarek, and D. Erni, *J. Lightwave Technol.* **16**, 1680–1685 (1998).
- [56] M. Palamaru and P. Lalanne, *Appl. Phys. Lett.* **78**, 1466–1468 (2001).
- [57] P. Lalanne and A. Talneau, *Opt. Express* **10**, 354–359 (2002).
- [58] Map of Life, Corneal nipple arrays in insect eyes, February 2014.
- [59] D. C. Flanders, *Appl. Phys. Lett.* **42**, 492–494 (1983).
- [60] Y. Ono, Y. Kimura, Y. Ohta, and N. Nishida, *Appl. Opt.* **26**, 1142–1146 (1987).
- [61] P. Lalanne and G. M. Morris, *Nanotechnology* **8**, 53–56 (1997).
- [62] Y. Kanamori, M. Sasaki, and K. Hane, *Opt. Lett.* **24**, 1422–1424 (1999).
- [63] H. Kikuta, H. Toyota, and W. Yu, *Opt. Rev.* **10**, 63–73 (2003).
- [64] P. Cheben, D. X. Xu, S. Janz, and A. Delâge, *Proc. SPIE* **5117**, 147–156 (2003).
- [65] S. Janz, A. Balakrishnan, S. Charbonneau, P. Cheben, M. Cloutier, A. Delage, K. Dossou, L. Erickson, M. Gao, P. Krug, B. Lamontagne, M. Packirisamy, M. Pearson, and D. X. Xu, *IEEE Photonics Technol. Lett.* **16**, 503–505 (2004).
- [66] D. Pérez-Galacho, R. Halir, A. Ortega-Moñux, C. Alonso-Ramos, R. Zhang, P. Runge, K. Janiak, H. G. Bach, A. Steffan, and I. Molina-Fernández, *Opt. Express* **21**, 14146–14151 (2013).
- [67] J. Schmid, P. Cheben, S. Janz, J. Lapointe, E. Post, and D. X. Xu, *Opt. Lett.* **32**, 1794–1796 (2007).
- [68] V. R. Almeida, Q. Xu, C. A. Barrios, and M. Lipson, *Opt. Lett.* **29**, 1209–1211 (2004).
- [69] Q. Xu, V. R. Almeida, R. R. Panepucci, and M. Lipson, *Opt. Lett.* **29**, 1626–1628 (2004).
- [70] F. Dell’Olio and V. M. Passaro, *Opt. Express* **15**, 4977–4993 (2007).
- [71] C. A. Barrios, K. B. Gylfason, B. Sánchez, A. Griol, H. Söhlström, M. Holgado, and R. Casquel, *Opt. Lett.* **32**, 3080–3082 (2007).
- [72] S. H. Yang, M. L. Cooper, P. R. Bandaru, and S. Mookherjea, *Opt. Express* **16**, 8306–8316 (2008).
- [73] A. V. Velasco, M. L. Calvo, P. Cheben, A. Ortega-Moñux, J. H. Schmid, C. A. Ramos, Í. M. Fernandez, J. Lapointe, M. Vachon, S. Janz, and D. X. Xu, *Opt. Lett.* **37**, 365–367 (2012).
- [74] B. Holmes and D. Hutchings, *IEEE Photonics Technol. Lett.* **18**, 43–45 (2006).
- [75] W. Stork, N. Streibl, H. Haidner, and P. Kipfer, *Opt. Lett.* **16**, 1921–1923 (1991).
- [76] F. Chen and H. Craighead, *Opt. Lett.* **20**, 121–123 (1995).
- [77] P. Kipfer, M. Collischon, H. Haidner, and J. Schwider, *Opt. Eng.* **35**, 726–731 (1996).
- [78] P. Lalanne, S. Astilean, P. Chavel, E. Cambril, and H. Launois, *Opt. Lett.* **23**, 1081–1083 (1998).
- [79] U. Levy, M. Nezhad, H. C. Kim, C. H. Tsai, L. Pang, and Y. Fainman, *J. Opt. Soc. Am. A* **22**, 724–733 (2005).
- [80] U. Levy, M. Abashin, K. Ikeda, A. Krishnamoorthy, J. Cunningham, and Y. Fainman, *Phys. Rev. Lett.* **98**, 243901 (2007).
- [81] H. Kurt and D. S. Citrin, *Opt. Express* **15**, 1240–1253 (2007).
- [82] M. Grajower, G. M. Lerman, I. Goykhman, B. Desiatov, A. Yanai, D. R. Smith, and U. Levy, *Opt. Lett.* **38**, 3492–3495 (2013).
- [83] M. Born and E. Wolf, *Principles of Optics: Electromagnetic Theory of Propagation, Interference and Diffraction of Light* (Cambridge University Press, Cambridge, 1999).
- [84] J. Valentine, J. Li, T. Zentgraf, G. Bartal, and X. Zhang, *Nat. Mater.* **8**, 568–571 (2009).
- [85] E. Cassan and K. V. Do, *J. Opt. Soc. Am. B* **28**, 1905–1910 (2011).
- [86] H. Gao, B. Zhang, S. G. Johnson, and G. Barbastathis, *Opt. Express* **20**, 1617–1628 (2012).
- [87] X. Chen and H. Tsang, *IEEE Photonics J.* **1**, 184–190 (2009).
- [88] L. Liu, M. Pu, K. Yvind, and J. M. Hvam, *Appl. Phys. Lett.* **96**, 051126 (2010).
- [89] R. Halir, P. Cheben, J. Schmid, R. Ma, D. Bedard, S. Janz, D. X. Xu, A. Densmore, J. Lapointe, and I. Molina-Fernández, *Opt. Lett.* **35**, 3243–3245 (2010).
- [90] J. Yang, Z. Zhou, H. Jia, X. Zhang, and S. Qin, *Opt. Lett.* **36**, 2614–2617 (2011).
- [91] X. Chen and H. K. Tsang, *Opt. Lett.* **36**, 796–798 (2011).
- [92] R. Halir, L. Zavargo-Peche, D. X. Xu, P. Cheben, R. Ma, J. Schmid, S. Janz, A. Densmore, A. Ortega-Moñux, I. Molina-Fernández, M. Fournier, and J.-M. Fédeli, *Opt. Quantum Electron.* **44**, 521–526 (2012).
- [93] H. Subbaraman, X. Xu, J. Covey, and R. T. Chen, *Opt. Express* **20**, 20659–20665 (2012).
- [94] X. Xu, H. Subbaraman, J. Covey, D. Kwong, A. Hosseini, and R. T. Chen, *Appl. Phys. Lett.* **101**, 031109 (2012).

- [95] X. Chen, K. Xu, Z. Cheng, C. K. Fung, and H. K. Tsang, *Opt. Lett.* **37**, 3483–3485 (2012).
- [96] Z. Cheng, X. Chen, C. Yan Wong, K. Xu, and H. Ki Tsang, *Opt. Lett.* **37**, 5181–5183 (2012).
- [97] K. Qin, D. Gao, C. Bao, Z. Zhao, X. Zhou, T. Lu, and L. Chen, *J. Lightwave Technol.* **30**, 2363–2366 (2012).
- [98] Z. Cheng, X. Chen, C. Wong, K. Xu, C. K. Fung, Y. Chen, and H. K. Tsang, *IEEE Photonics J.* **4**, 104–113 (2012).
- [99] Z. Cheng, X. Chen, C. Y. Wong, K. Xu, and H. K. Tsang, *Appl. Phys. Lett.* **101**, 101104 (2012).
- [100] X. Xu, H. Subbaraman, J. Covey, D. Kwong, A. Hosseini, and R. T. Chen, *Opt. Lett.* **38**, 3588–3591 (2013).
- [101] Y. Ding, H. Ou, and C. Peucheret, *Opt. Lett.* **38**, 2732–2734 (2013).
- [102] Z. Cheng and H. Tsang, *Opt. Lett.* **39**, 2206–2209 (2014).
- [103] C. Alonso-Ramos, A. Ortega-Moñux, I. Molina-Fernández, P. Cheben, L. Zavargo-Peché, and R. Halir, *Opt. Express* **18**, 15189–15200 (2010).
- [104] R. Waldhäusl, B. Schnabel, P. Dannberg, E. B. Kley, A. Bräuer, and W. Karthe, *Appl. Opt.* **36**, 9383–9390 (1997).
- [105] F. Van Laere, T. Claes, J. Schrauwen, S. Scheerlinck, W. Bogaerts, D. Taillaert, L. O’Faolain, D. Van Thourhout, and R. Baets, *IEEE Photonics Technol. Lett.* **19**, 1919–1921 (2007).
- [106] F. Van Laere, G. Roelkens, M. Ayre, J. Schrauwen, D. Taillaert, D. Van Thourhout, T. F. Krauss, and R. Baets, *J. Lightwave Technol.* **25**, 151–156 (2007).
- [107] C. Alonso-Ramos, L. Zavargo-Peché, A. Ortega-Moñux, R. Halir, I. Molina-Fernández, and P. Cheben, *Opt. Lett.* **37**, 3663–3665 (2012).
- [108] W. S. Zaoui, A. Kunze, W. Vogel, M. Berroth, J. Butschke, F. Letzkus, and J. Burghartz, *Opt. Express* **22**, 1277–1286 (2014).
- [109] T. Aoyagi, Y. Aoyagi, and S. Namba, *Appl. Phys. Lett.* **29**, 303 (1976).
- [110] M. Fan, M. Popovic, and F. X. Kärtner, in: Proceedings of the Conference on Lasers and Electro-Optics, Baltimore, MD, 6–11 May 2007.
- [111] G. Roelkens, D. Van Thourhout, and R. Baets, *Opt. Express* **14**, 11622–11630 (2006).
- [112] D. X. Xu, J. Schmid, G. Reed, G. Mashanovich, D. Thomson, M. Nedeljkovic, X. Chen, D. Van Thourhout, S. Keyvaninia, and S. Selvaraja, *IEEE J. Select. Topics Quantum Electron.* **20**, 8100217 (2014).
- [113] D. Taillaert, H. Chong, P. I. Borel, L. H. Frandsen, R. De La Rue, and R. Baets, *IEEE Photonics Technol. Lett.* **15**, 1249–1251 (2003).
- [114] W. S. Zaoui, A. Kunze, W. Vogel, and M. Berroth, *IEEE Photonics Technol. Lett.* **25**, 1395–1397 (2013).
- [115] C. Alonso-Ramos, L. Zavargo-Peché, A. Ortega-Moñux, R. Halir, I. Molina-Fernández, and P. Cheben, *Opt. Lett.* **37**, 3663–3665 (2012).
- [116] R. Soref, *Nat. Photonics* **4**, 495–497 (2010).
- [117] P. J. Bock, P. Cheben, A. Delâge, J. H. Schmid, D. X. Xu, S. Janz, and T. J. Hall, *Opt. Express* **16**, 17616–17625 (2008).
- [118] P. J. Bock, P. Cheben, J. H. Schmid, A. V. Velasco, A. Delâge, S. Janz, D. X. Xu, J. Lapointe, T. J. Hall, and M. L. Calvo, *Opt. Express* **20**, 19882–19892 (2012).
- [119] Y. Ding and R. Magnusson, *Opt. Express* **12**, 1885–1891 (2004).
- [120] Y. Ding and R. Magnusson, *Opt. Express* **12**, 5661–5674 (2004).
- [121] P. Lalanne, J. P. Hugonin, and P. Chavel, *J. Lightwave Technol.* **24**, 2442–2449 (2006).
- [122] V. Karagodsky and C. J. Chang-Hasnain, *Opt. Express* **20**, 10888–10895 (2012).
- [123] R. Magnusson and S. Wang, *Appl. Phys. Lett.* **61**, 1022–1024 (1992).
- [124] D. L. Brundrett, E. N. Glytsis, and T. K. Gaylord, *Opt. Lett.* **23**, 700–702 (1998).
- [125] Y. Kanamori, M. Shimono, and K. Hane, *IEEE Photonics Technol. Lett.* **18**, 2126–2128 (2006).
- [126] P. Cheben, S. Janz, D. X. Xu, B. Lamontagne, A. Delâge, and S. Taney, *IEEE Photonics Technol. Lett.* **18**, 13–15 (2006).
- [127] B. W. Yoo, M. Megens, T. Chan, T. Sun, W. Yang, C. J. Chang-Hasnain, D. A. Horsley, and M. C. Wu, *Opt. Express* **21**, 12238–12248 (2013).
- [128] A. Liu, F. Fu, Y. Wang, B. Jiang, and W. Zheng, *Opt. Express* **20**, 14991–15000 (2012).
- [129] S. Y. Chou and W. Deng, *Appl. Phys. Lett.* **67**, 742–744 (1995).
- [130] R. Magnusson, M. Shokoh-Saremi, and E. G. Johnson, *Opt. Lett.* **35**, 2472–2474 (2010).
- [131] K. J. Lee and R. Magnusson, *IEEE Photonics J.* **3**, 123–129 (2011).
- [132] F. T. Chen and H. G. Craighead, *Opt. Lett.* **21**, 177–179 (1996).
- [133] D. Fattal, J. Li, Z. Peng, M. Fiorentino, and R. G. Beausoleil, *Nat. Photonics* **4**, 466–470 (2010).
- [134] C. Chase, Y. Zhou, and C. J. Chang-Hasnain, *Opt. Express* **17**, 24002–24007 (2009).
- [135] M. C. Huang, Y. Zhou, and C. J. Chang-Hasnain, *Nat. Photonics* **2**, 180–184 (2008).
- [136] Y. Rao, W. Yang, C. Chase, M. Huang, D. Worland, S. Khaleghi, M. Chitgarha, M. Ziyadi, A. Willner, and C. Chang-Hasnain, *IEEE J. Select. Topics Quantum Electron.* **19**, 1701311 (2013).
- [137] I. S. Chung, V. Iakovlev, A. Sirbu, A. Mereuta, A. Caliman, E. Kapon, and J. Mork, *IEEE J. Quantum Electron.* **46**, 1245–1253 (2010).
- [138] Y. Zhou, M. C. Huang, and C. J. Chang-Hasnain, *IEEE Photonics Technol. Lett.* **20**, 434–436 (2008).
- [139] M. Gebski, M. Dems, J. Chen, Q. Wang, D. Zhang, and T. Czyszanowski, *J. Lightwave Technol.* **31**, 3853–3858 (2013).
- [140] C. Sciancalepore, B. B. Bakir, X. Letartre, J. M. Fedeli, N. Olivier, D. Bordel, C. Seassal, P. Rojo-Romeo, P. Regreny, and P. Viktorovitch, *J. Lightwave Technol.* **29**, 2015–2024 (2011).
- [141] M. Loncar, T. Doll, J. Vuckovic, and A. Scherer, *J. Lightwave Technol.* **18**, 1402–1411 (2000).
- [142] S. Ha, A. A. Sukhorukov, D. A. Powell, I. V. Shadrivov, A. V. Lavrinenko, D. N. Chigrin, and Y. S. Kivshar, in: *Frontiers in Optics 2008* (Optical Society of America, 2008), paper FWL3.
- [143] S. Ha, A. A. Sukhorukov, K. B. Dossou, L. C. Botten, A. V. Lavrinenko, D. N. Chigrin, and Y. S. Kivshar, *Opt. Express* **16**, 1104–1114 (2008).

- [144] P. J. Bock, P. Cheben, J. H. Schmid, J. Lapointe, A. Delâge, S. Janz, G. C. Aers, D. X. Xu, A. Densmore, and T. J. Hall, Opt. Express **18**, 20251–20262 (2010).
- [145] W. Śmigaj, P. Lalanne, J. Yang, T. Paul, C. Rockstuhl, and F. Lederer, Appl. Phys. Lett. **98**, 111107 (2011).
- [146] J. Schmid, M. Ibrahim, P. Cheben, J. Lapointe, S. Janz, P. Bock, A. Densmore, B. Lamontagne, R. Ma, W. Ye, and D.-X. Xu, Opt. Lett. **36**, 2110–2112 (2011).
- [147] M. Ibrahim, J. H. Schmid, A. Aleali, P. Cheben, J. Lapointe, S. Janz, P. J. Bock, A. Densmore, B. Lamontagne, R. Ma, D.-X. Xu, and W. N. Ye, Opt. Express **20**, 18356–18361 (2012).
- [148] K. Watanabe, Y. Hashizume, Y. Nasu, Y. Sakamaki, M. Kohtoku, M. Itoh, and Y. Inoue, Electron. Lett. **44**, 1356–1357 (2008).
- [149] A. V. Tsarev, Opt. Express **19**, 13732–13737 (2011).
- [150] M. A. Popović, E. P. Ippen, and F. X. Kärtner, in: Proceedings of the 20th Annual Meeting of the IEEE Lasers and Electro-Optics Society, Lake Buena Vista, FL, 21–25 October 2007, pp. 56–57.
- [151] Y. Liu, J. M. Shainline, X. Zeng, and M. A. Popović, Opt. Lett. **39**, 335–338 (2014).
- [152] S. G. Johnson, C. Manolatou, S. Fan, P. R. Villeneuve, J. Joannopoulos, and H. Haus, Opt. Lett. **23**, 1855–1857 (1998).
- [153] Y. Zhang, A. Hosseini, X. Xu, D. Kwong, and R. T. Chen, Opt. Lett. **38**, 3608–3611 (2013).
- [154] P. Cheben, D. X. Xu, S. Janz, and A. Densmore, Opt. Express **14**, 4695–4702 (2006).
- [155] V. R. Almeida, R. R. Panepucci, and M. Lipson, Opt. Lett. **28**, 1302–1304 (2003).
- [156] D. Pérez-Galacho, R. Halir, L. F. Zavargo-Peché, J. G. Wangüemert-Pérez, A. Ortega-Moñux, I. Molina-Fernández, and P. Cheben, in: Proceedings of the European Conference on Integrated Optics, Barcelona, Spain, 18–20 April 2012, paper 71.
- [157] J. Ctyroky, P. Kwiecien, I. Richter, and P. Cheben, Proc. SPIE **8781**, 87810B (2013).
- [158] P. J. Bock, P. Cheben, J. H. Schmid, A. Delâge, D. X. Xu, S. Janz, and T. J. Hall, Opt. Express **17**, 19120–19133 (2009).
- [159] M. Florjanczyk, P. Cheben, S. Janz, A. Scott, B. Solheim, and D. X. Xu, Opt. Express **15**, 18176–18189 (2007).
- [160] P. J. Bock, P. Cheben, A. V. Velasco, J. H. Schmid, A. Delâge, M. Florjanczyk, J. Lapointe, D. X. Xu, M. Vachon, S. Janz, and M. L. Calvo, Laser Photonics Rev. **7**, L67–L70 (2013).
- [161] A. V. Velasco, P. Cheben, P. J. Bock, A. Delâge, J. H. Schmid, J. Lapointe, S. Janz, M. L. Calvo, D. X. Xu, M. Florjanczyk, and M. Vachon, Opt. Lett. **38**, 706–708 (2013).
- [162] I. Glesk, P. Bock, P. Cheben, J. Schmid, J. Lapointe, and S. Janz, Opt. Express **19**, 14031–14039 (2011).
- [163] S. Akiyama, M. Imai, T. Baba, T. Akagawa, N. Hirayama, Y. Noguchi, M. Seki, K. Koshino, M. Toyama, T. Horikawa, and T. Usuki, IEEE J. Select. Topics Quantum Electron. **19**, 3401611 (2013).
- [164] D. X. Xu, A. Densmore, P. Waldron, J. Lapointe, E. Post, A. Delâge, S. Janz, P. Cheben, J. H. Schmid, and B. Lamontagne, Opt. Express **15**, 3149–3155 (2007).
- [165] R. Halir, G. Roelkens, A. Ortega-Moñux, and J. Wangüemert-Pérez, Opt. Lett. **36**, 178–180 (2011).
- [166] R. Halir, L. Vivien, X. Le Roux, D. X. Xu, and P. Cheben, IEEE Photonics J. **5**, 6800906 (2013).
- [167] L. B. Soldano and E. C. Pennings, J. Lightwave Technol. **13**, 615–627 (1995).
- [168] Z. Huang, R. Scarmozzino, and R. Osgood, IEEE Photonics Technol. Lett. **10**, 1292–1294 (1998).
- [169] A. Ortega-Moñux, L. Zavargo-Peché, A. Maese-Novo, I. Molina-Fernández, R. Halir, J. Wangüemert-Pérez, P. Cheben, and J. Schmid, IEEE Photonics Technol. Lett. **23**, 1406–1408 (2011).
- [170] Optical Internetworking Forum, physical and link layer (PLL) working group, Implementation agreement for integrated dual polarization intradyne coherent receivers (2011).
- [171] T. Föhn, W. Vogel, M. Schmidt, M. Berroth, J. Butschke, and F. Letzkus, in: Proceedings of the Optical Fiber Communication Conference, San Francisco, CA, 9–13 March 2014 (Optical Society of America, 2014), paper Th3F4.
- [172] D. M. Mackie and A. W. Lee, Appl. Opt. **43**, 6609–6619 (2004).
- [173] J. Campbell and T. Li, J. Appl. Phys. **50**, 6149–6154 (1979).
- [174] A. Ortega-Moñux, C. Alonso-Ramos, A. Maese-Novo, R. Halir, L. Zavargo-Peché, D. Pérez-Galacho, I. Molina-Fernández, J. G. Wangüemert-Pérez, P. Cheben, J. H. Schmid, J. Lapointe, D. Xu, and S. Janz, Laser Photonics Rev. **7**, L12–L15 (2013).
- [175] Y. Shani, C. H. Henry, R. C. Kistler, R. F. Kazaninov, and K. J. Orlowsky, IEEE J. Quantum Electron. **27**, 556–566 (1991).
- [176] G. T. Paloczi, A. Eyal, and A. Yariv, IEEE Photonics Technol. Lett. **16**, 515–517 (2004).
- [177] C. Doerr, M. Cappuzzo, E. Chen, A. Wong-Foy, L. Gomez, A. Griffin, and L. Buhl, IEEE Photonics Technol. Lett. **17**, 1211–1213 (2005).
- [178] M. Alam, J. N. Caspers, J. Aitchison, and M. Mojahedi, Opt. Express **21**, 16029–16034 (2013).
- [179] R. Halir, A. Maese-Novo, A. Ortega-Moñux, I. Molina-Fernández, J. Wangüemert-Pérez, P. Cheben, D. Xu, J. Schmid, and S. Janz, Opt. Express **20**, 13470–13477 (2012).